7/-47

p. 47

FINAL PROJECT REPORT for

NASA Award Number NAG5-1153

"Measurement of the Sizes of Circumstellar Dust Shells Around Evolved Stars with High Mass Loss Rates"

6/15/89-11/30/91

T. G. Phillips, Principal Investigator
California Institute of Technology
Division of Physics, Mathematics and Astronomy
Mail Code 320-47, Downs Laboratory
Pasadena, CA 91125

G. R. Knapp, Co-Investigator
Department of Astrophysical Sciences
Princeton University
Princeton, NJ 08544

January 9, 1992

Measurement of the Sizes of Circumstellar Dust Shells Around Evolved Stars with High Mass Loss Rates II

Final Project Report

T.G. Phillips, Principal Investigator, 320-47 Caltech, Pasadena, CA 91125
G.R. Knapp, Department of Astrophysical Sciences, Princeton University, Princeton, NJ 08544

The research supported by the NASA ADP contract NAG 5–1153 has been completed. The attached paper, which will be submitted for publication in the *Astrophysical Journal* in January 1992, presents the results of this work.

Here is a summary of the project and its results. A set of computer programs was developed to process the raw 60μ and 100μ *IRAS* survey data. The programs were designed to detect faint extended emission surrounding a bright unresolved source. Candidate objects were chosen from a list of red giant stars and young planetary nebulae which have been detected in millimeter/submillimeter lines of CO. Of the 279 stars examined, 55 where resolved at 60μ. The principle results of the study are:

- The average age for the shells surrounding the 9 Mira–type stars which are extended is 6×10^4 yr. This suggests that the period during which these stars lose mass lasts for $\sim 10^5$ yr. The oldest shell found surrounds U Ori, and the youngest surrounds Mira itself.

- Some shells appear to be detached from the central star. This phenomenon is more common among older stars, suggesting that the mass loss process becomes more episodic as the star sheds its envelope. This might be caused by the the star's thermal pulse cycle, which has an increasingly pronounced effect on the stellar atmosphere as the envelope mass decreases.

- Although all 8 stars less distant than 200 pc are resolved in the *IRAS* 60μ data, 29 stars within 500 pc were not. These stars probably have younger circumstellar shells than those which were resolved.

- Almost all the carbon stars with distances of 500 pc or less have resolved shells, while only 1/2 of the oxygen–rich stars do. The resolved carbon star shells also are older on average than the oxygen–rich ones. These facts imply that carbon stars have been losing mass for a longer period, on average, than oxygen–rich red giants. The average age of these nearby carbon stars is 8.6×10^4 yr, which indicates the lifetime of an average carbon star is 1.5×10^5 yr.

- Large circumstellar shells tend to be found at large distances from the galactic plane, confirming that the ISM density limits the size to which a dust shell can grow. Surprisingly, even very large shells seem to be nearly spherical, and do not appear to be distorted by ram–pressure caused by the star's motion with respect to the ISM.

- Radiative transfer models and the value of $I_{60\mu}/I_{100\mu}$ allow the average dust temperature in the outer regions of a circumstellar shell to be estimated. The typical value obtained is about 35 K. This provides a constraint on the value of the dust drift velocity, because a very large drift velocity results in a low dust density in the outer shell which in turn requires a high dust temperature to produce the 60μ and 100μ fluxes measured by *IRAS*. The radial dependence of $I_{60\mu}/I_{100\mu}$ suggests that an external heat source supplies most of the thermal energy to the dust beyond a radius of 1 pc.

Circumstellar Shells Resolved in IRAS Survey Data

K. Young[1], *T.G. Phillips*[1] *and G.R. Knapp*[2]

[1]California Institute of Technology, Pasadena, CA 91125

[2]Department of Astrophysical Sciences, Princeton University, Princeton, NJ 08544

ABSTRACT

The *IRAS* survey data for 279 red giant stars and young planetary nebulae, which have been detected in rotational transitions of CO, were examined. Of these stars 55 were found to have a circumstellar shell (CSS) that is resolved in the 60μ survey data. Some of these stars are also resolved in the 100μ survey data. Approximately half of the 55 stars are carbon stars. Two of the carbon stars, W Pic and RY Dra, have shells with radii of 3 pc or more. No evidence was found that the shapes of the shells were distorted by interaction with the ISM, however the size of the shells does appear to depend on the local ISM density, and therefore on the distance from the star to the galactic plane. The average dust temperature in the outer region of the shells is $\sim$ 35 K. Using this temperature and the mass loss rates derived from observations of the inner shell, it is shown that the expansion velocity of the dust cannot greatly exceed that of the gaseous material. Some of the shells appear to be detached from the central star. Detached shells tend to be older than average, suggesting that mass loss becomes more episodic as the object ages. Analysis of the colors of the shells resolved in both the 60μ and 100μ bands shows that the central star is the dominant dust heating source at radii less than $\sim$ 1 pc, whereas an external source dominates at larger radii. Nine of the stars found to be extended are Mira variables. A simple model of the evolution of these shells suggests that the period during which Mira variables lose mass lasts for $\sim 10^5$ years. For the largest shells the expansion velocity of the outer shell will typically be lower than the expansion velocity obtained from CO observations, by a factor of 3–5.

Subject headings: stars: mass–loss — stars: evolution — stars: circumstellar matter — stars: variables: Miras

1. Introduction

Much of the mass returned to the interstellar medium by stellar evolution processes is shed during the asymptotic giant branch (AGB) stage. AGB stars are cool ($T_{eff} \leq$ 2000 K) and very luminous ($L_{bol} \sim 10^4\ L_\odot$), and are observed to shed mass copiously (mass loss rates in the range 10^{-8} to $10^{-4}\ M_\odot\ yr^{-1}$ are observed). Since the stars are cool, the mass is shed in the form of molecules and dust, and can therefore be studied at radio, millimeter and infrared wavelengths. Studies of the mass shed by evolved stars are important for understanding stellar evolution, the formation of planetary nebulae, and the evolution of the interstellar medium in the Galaxy. The focus of the work presented here is on measuring the angular extent of the emission from circumstellar dust in these envelopes. The outflow velocity is given by molecular line observations; together with an estimate of the distance, the envelope extent yields the linear size and age of the envelope. Since the molecular line observations

also give estimates of the stellar mass-loss rate, the total envelope mass can be found. We can then obtain a lower limit for the mass lost by these stars (which, given data on a large enough sample of objects, can be used to give an estimate of the total mass returned to the interstellar medium).

At first sight, it might be thought that these goals could be accomplished by mapping the millimeter wavelength molecular line emission, but the sizes of molecular envelopes are truncated by photodissociation (Letzelter *et al.* 1987; Mamon *et al.* 1988). Also, although HI is not photodestroyed in the normal interstellar radiation field, the 21 cm emission from the circumstellar shells is extremely weak, and HI is ubiquitous and strong in the Galactic disk, so that HI observations are of very limited utility for this work.

The *IRAS* Point Source Catalog (IRAS, 1985; hereafter PSC) contains some 246,000 detections, of which about 81,000 have colors suggesting the presence of circumstellar emission (Olofsson, 1988, van der Veen 1988). We wished to determine which of these stars had a CSS which had been spatially resolved in the *IRAS* survey. An AGB star with a luminosity of $10^4 L_\odot$ could be as distant as 10 kpc, and still have a 60μ flux density above the PSC cutoff of 0.5 Jy. However since a typical large CSS is expected to have a radius of about .3 pc (Rowan-Robinson *et al.* 1986), it must be no further than 1 kpc to be resolved by the 60" beam *IRAS* provided at 60μ. We therefore needed a way to select the small percentage of AGBs in the PSC which were nearby and had large circumstellar envelopes. We chose to examine only those stars which have been detected in a rotational transition of CO. Such a star must be relatively nearby and have a large envelope, or else telescope beam-dilution would prevent detection of its molecular line emission. In addition, the CO observations provide a direct measurement of the inner envelope's outflow velocity and an estimate of the star's mass loss rate, both of which are needed to estimate the age of a CSS.

2. Data Processing

The primary goal of the *IRAS* project was to survey the entire sky at 4 infrared wavelengths. While some specific objects were studied individually by the satellite, most of the sky was only observed as part of the all–sky survey. The overriding consideration in the design of the survey was to ensure the reliability of the derived data products; the Point Source Catalog, the Small Scale Structure Catalog, the Atlas of Low–Resolution Spectra and the maps of total sky brightness. A major difficultly in ensuring the integrity of these products was that the unprocessed survey data is contaminated with "detections" caused by cosmic rays, earth–orbiting debris and minor denizens of the solar system. In order to recognize and reject these spurious detections, the survey was designed to observe each position in the sky several times. For this reason, the *IRAS* survey data for a particular object consists of one or more sets of detector scans passing near the object's position.

Because the *IRAS* survey was designed to produce reliable measurements of new objects, rather than to carry out detailed studies of well–known objects, there are several characteristics of the survey data which make it difficult to produce high–resolution images from the scans. The individual *IRAS* detectors were larger than the telescope's diffraction pattern, particularly in the direction parallel to the satellite's rotation axis (the "cross-scan" direction). Only by analyzing the data from several detectors, whose paths on the sky partially overlap, can information about source structure on spatial scales near the instrument's diffraction be recovered. Also, the detectors' outputs were passed through low–pass filters with cutoff frequencies well below the frequencies required for Nyquist sampling when the satellite was scanning the sky at the survey rate.

Instead of deconvolving the *IRAS* data and producing a map, we fitted a model of a point source surrounded by dust to the data. There were two reasons for doing this. First, the sky coverage of *IRAS* data is non-uniform. In some cases (about 10%), the survey data covers the object with scans approaching the star from several different position angles. In these cases it should be possible to construct a map of the circumstellar material. More commonly, the survey data consists of several sets of scans, all approaching the star with very nearly identical position angles. This fact, combined with the saturation which may occur as soon as the star's image falls upon the detector, makes it difficult to construct a two dimensional map of the material surrounding the star. On the other hand, since the detectors are extended in the cross scan direction, and since the distance of closest approach of each detector to the star's position varies, some two dimensional information is contained in the survey data even if each detector approaches with the same position angle. The second reason for fitting a model, rather than producing an image,

is that this approach directly gives values for the physically important parameters, such as the size and intensity of the dust shell's emission.

The data were fitted to a model consisting of an ellipsoidal envelope, at a single temperature throughout, with an unresolved point source at its center. Two of the axes of the ellipsoid were forced to be equal. The emission is proportional to the column density of the dust, and the density of the dust is assumed to decrease linearly with the square of the distance from the star, but at differing rates along the different axes of the ellipsoid. The intensity of emission from the dust alone at position *(x,y)* is

$$I(x,y) = \frac{C}{\sqrt{k^2x^2+y^2}} \arctan\left(\sqrt{\frac{b^2-k^2x^2-y^2}{k^2x^2+y^2}}\right)$$

where

x	= the distance from the model center along the semimajor axis
y	= the distance from the model center along the semiminor axis
C	= a constant proportional to the rate of mass loss in dust (a model parameter)
k	= the ratio of the minor axis length to the major axis length (a model parameter)
b	= the semiminor axis length (a model parameter)

Since the formula above gives an infinite result at (0,0), the model assumes that the emission from dust reaches a constant value along lines of sight intersecting some inner radius where either the envelope is terminated, or the dust becomes optically thick. This inner radius is another parameter fitted by the model fitting program (MFP).

In addition to the parameters C, k and b of the dust model above, the model includes the intensity of the star, the RA and Dec offsets of the model from the position given to ADDSCAN (an IPAC program which originally extracted the data), and a position angle in the sky of the major axis of the envelope, as parameters to be determined.

The model is fitted by minimizing the function

$$error = \sum_{i=1}^{N_D} \sum_{j=1}^{N_{S_i}} \sum_{k=1}^{N_{P_{ij}}} \left| \frac{y_{ijk} - y_{ijk}(\vec{a})}{\sigma_i} \right|$$

where

N_D	= the number of *IRAS* detectors for a particular band
N_{S_i}	= the number of scans for this source from detector i
$N_{P_{ij}}$	= the number of points in the j^{th} scan of the i^{th} detector
y_{ijk}	= the k^{th} data point from the j^{th} scan of the i^{th} detector
σ_i	= the noise level of the i^{th} detector relative to other detectors
$\vec{a}$	= a vector composed of the eight model parameters

$y_{ijk}(\vec{a})$ is a two dimensional integral of the model intensity at the sky position corresponding to y_{ijk} multiplied by the response function for the i^{th} detector

$$y_{ijk}(\vec{a}) = \int_{-S_i}^{S_i} \int_{-T_i}^{T_i} I(\vec{a},s,t) R_i(s,t) ds dt$$

The limits in the integral above correspond to the spatial extent of the i^{th} detector, which for the 60μ detectors is $\pm$3.0' in the in-scan direction and $\pm$3.3' in the cross-scan direction. $R_i(s,t)$, the 2 dimensional response function of the i^{th} detector, is calculated from the Moshir response functions (Moshir, 1989). These response functions were

derived from a set of 32 Additional Observations (AOs) of the planetary nebula NGC 6543. The functions do not perfectly represent the point spread function of the *IRAS* detectors during survey observations, for two reasons. The first reason is that NGC 6543 was slightly resolved by *IRAS*. The second reason is that when the AO data were taken, the satellite scanned the sky more slowly than it did during survey observations. Since the detector outputs where passed through low–pass filters, and since the detectors themselves were hysteretic, the response functions derived from AOs are less extended on the sky than a point source observed at the survey scan rate would be. Since the first problem makes the templates too large on the sky, and the second makes them too small, the problems cancel each other to some extent. Tests, described below, were performed to judge how well the Moshir functions mimicked the shape of a point source observed during the survey. $y_{ijk}(\vec{a})$ was calculated by Simpson's rule integration. The function *error* was minimized in the eight dimensional space of model parameters by a direction set algorithm (Press 1986). The integrals were calculated to a precision of 5%, and the direction set algorithm was iterated until an iteration passed during which none of the model parameters changed by as much as 5%.

The absolute value of the deviation of the model from the data was minimized, rather than the square of the deviation, which is a more common figure of merit. This approach was taken because the noise in *IRAS* data is very non-Gaussian. Radiation hits and emission from dust near the satellite produced frequent spikes in the data, which have a noticeable effect on the MFP if the square of the deviation is used as the figure of merit.

2.1 Data Processing Steps

Of the four *IRAS* bands, dust emission is visible primarily in the 60μ and 100μ data, where the emission from the central star is less dominant. The 60μ data was analysed first, because the 60μ data yields higher resolution and is much less effected by infrared cirrus emission. The stars to be analysed were selected from a list of evolved stars which have been detected in at least one rotational line of CO. Each star's data set was produced by the default ADDSCAN processing, and consists of all scans in which the star passes within 1.7' of the detector center.

The first step in processing the data was to subtract a linear baseline from the Calibrated Raw Detector Data (CRDD). The baseline is fitted to 2 windows 15' away from the star's position. If one of the windows contained emission from another source, then the windows were moved further from the source to regions showing no emission. Obvious noise spikes were also removed at this point.

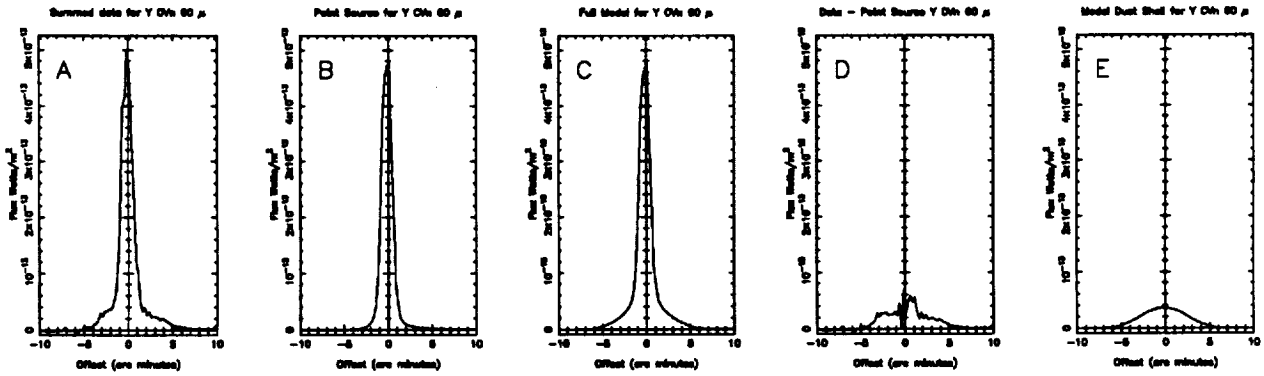

Fig. 1. (A) All the scans for the source Y CVn, averaged together. To produce this plot the data points were averaged in bins 15" wide. The bin in which to place a data point was determined by the distance of the point from the source, in the in-scan direction. (B) Results from the first pass of the model fitting program (MFP) are shown. Synthetic data were produced by calculating the flux predicted by the model for each point at which data was taken. The model used in this plot consisted of the MFP's best fit for the first three parameters: point source intensity, and RA and Dec offsets. (C) Results of the second pass of the MFP are shown. Synthetic data was produced, using the MFP's final best fit for both the point source and dust shell. (D) This plot shows the residual flux remaining after the best fit point source is subtracted from the data. Some residual

flux remains, form a resolved dust shell. (E) The rightmost plot shows synthetic data for the dust shell only.

The first pass of the MFP tried to fit just three of the model's eight parameters: the point source intensity, and the right ascension and declination offsets. After these three parameters were been determined, the MFP minimized the *error* function with respect to six parameters: point source intensity, dust shell density, radius at which dust becomes optically thick, semimajor axis length, aspect ratio, and position angle. The point source intensity had to be redetermined in this second fitting loop, because the first loop might have overestimated the intensity of the point source by ignoring the contribution from the resolved region. If MFP reported that the CSS extended as far as 15' from the star, the baseline windows were moved further from the central position and the data were reprocessed. Figure 1 compares the results of the two passes of the MFP to the CRDD data, for the case of the carbon star Y CVn.

For those objects which the MFP indicated were extended, the MFP was run a second time. For this run a larger data set was used, consisting of all scans which passed within 10' of the star's position. Figure 2 shows the increased coverage afforded by this larger data set, again for Y CVn. In the case of Y CVn, as with most of the stars, all the scans approached the star from nearly the same position angle. As a result of this, the extent of the dust in the direction perpendicular to the scans (the cross-scan direction) was very poorly constrained by the small data set. The larger data set allowed the size of the shell in the cross-scan direction to be determined much more accurately. This second 60μ processing pass was not performed for the four brightest resolved sources: CIT 6, α Ori, o Cet and IRC+10216. The CRDD data for these four objects shows optical cross–talk caused by the telescope's secondary support spider. None of these objects showed optical cross–talk in the 100μ band, except IRC+10216 which showed it only weakly.

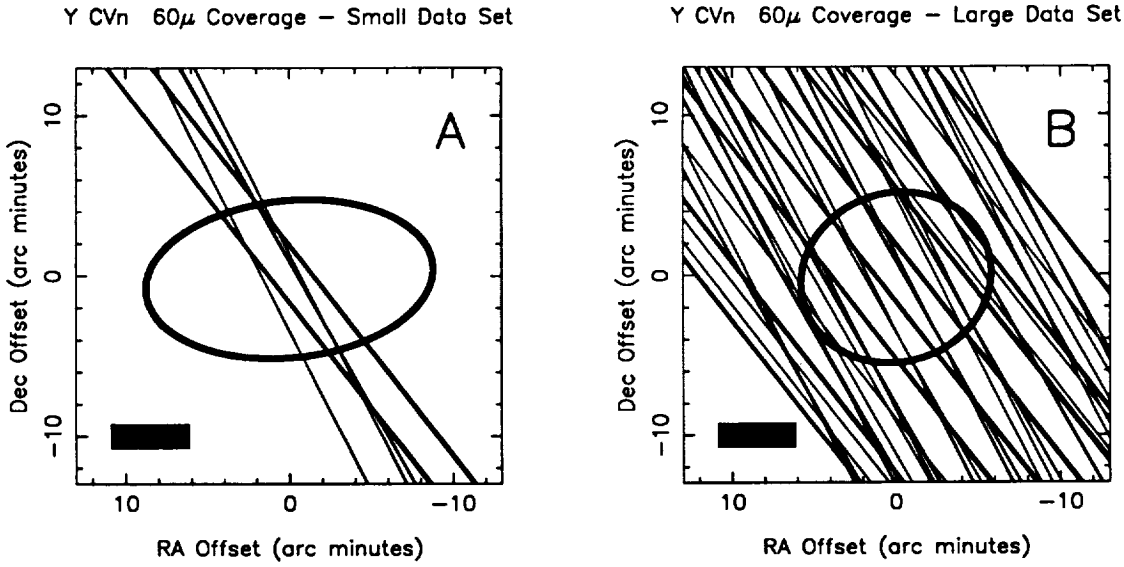

Fig. 2.

Figure A shows the coverage of the source Y CVn, using the default ADDSCAN selection criteria which selects all scans passing within 1.7' of the source. Each line represents the path on the sky of an *IRAS* detector, and some lines overlap. The ellipse plotted is the size and shape of the CSS, determined from these 10 scans. Since all the passes approached the source from nearly the same angle, the size of the dust shell in the orthogonal direction is poorly constrained. Figure B shows the increased coverage when all 56 scans which passed within 10' are used, along with the shape of the CSS derived from those scans. Even though all scans still approach from about the same angle, the size of the dust shell is now well constrained in all directions, and the CSS is seen to be nearly circular. In both figures, the black box shows the size of the largest *IRAS* 60μ detector.

Table 1. – Stars Examined and Rejected

Stars not observed during *IRAS* survey				
IRC–10236	NGC 7027	IRC+40483	IRC+00509	
Stars with curved baselines				
IRAS 00210+6221	OH 127.8 – 0.0	OH 141.7 + 3.5	U Ari	U Cam
RX Lep	IRC–10139	S Aur	S Ori	M 1 – 7
M 1 – 8	RY Mon	W CMa	IRC–20131	NGC 6072
RS Sco	RR Sco	IRAS 17217-3916	OH 09 + 1.3	TW Oph
OH 11.4 + 6.6	NGC 6445	IRAS 17581-1744	VX Sgr	NGC 6563
M 4 – 9	CRL 2154	IRAS 18248-0839	IRAS 18269-1257	OH 17.7 – 2.0
OH 26.5 + 0.6	IRC+00365	IRAS 18424+0346	R Sct	OH 30.1 – 0.7
S Sct	OH 32.8 – 0.3	OH 39.7 + 1.5	IRC+10401	V Aql
R Aql	IRAS 19068+0544	OH 44.8 – 2.3	Vy2 – 2	RT Aql
IRAS 19477+2401	IRAS 20028+3910	IRAS 20435+3825	IRAS 20532+5554	IRAS 21003+4801
V1549 Cyg	IRAS 21147+5110	IRAS 21223+5114	IRAS 21282+5050	IC 5117
IRAS 21318+5631	IRC+40485	RU Cyg	IRAS 21449+4950	M 2 – 51
OH 104.9 + 2.5	CRL 2985	CRL2999	CRL 3011	IRC+60427
Stars which were processed, but did not appear to be extended				
IRC+40004	T Cas	R And	IRC+10011	IRC+30021
IRC+60041	Z Psc	CRL 190	S Cas	W And
IRAS 02152+2822	R For	CRL 341	CIT 4	IRC–30023
R Hor	IRAS 03074-8732	TW Hor	CRL 482	OH 138.0 + 7.3
IRC+50096	CRL 5102	NML Tau	IRC+60144	CRL 618
IRAS 04530+4427	TX Cam	IRC+50137	NSV 1835	IRAS 05136+4712
IRC+60154	CRL 809	IRC+70066	Y Tau	IRC+40149
V Cam	CRL 865	TU Gem	CRL 933	CRL 935
CRL 954	IRC+60169	CRL 971	IRC–20101	GX Mon
CL Mon	R Vol	CRL 1085	IRAS 07134+1005	VY CMa
IRAS 07217-1246	S CMi	M 1 – 16	NGC 2440	OH 231.8 + 4.2
IRAS 07582-1933	IRAS 08045-1524	IRAS 08074-3615	CRL 1235	R Cnc
CRL 5250	W Cnc	CRL 5254	X Hya	IRAS 09371+1212
R LMi	IW Hya	X Vel	V Hya	IRAS 11308-1020
RU Vir	S Vir	CRL 4211	S CrB	IRAS 15194-5115
WX Ser	V CrB	R Ser	CRL 1822	RU Her
IRAS 16105-4205	U Her	g Her	M 2 – 9	CPD–56
CRL 1922	V463 Sco	NGC 6302	CRL 6815S	IRC+20326
MW Her	IRAS 17371-3021	CRL 5379	HD 161796	89 Her
T Dra	FX Ser	CRL 2135	CRL 2155	T Lyr
CRL 2199	IRC+10365	X Oph	IRC+20370	IRC+10374
IRAS 18467-4802	CRL 2259	IRC–30398	RS Cra	V3880 Sgr
IRC–30404	CRL 2343	W Aql	CRL 2362	IRC–10502
IRC+10420	CRL 2417	M1 – 92	IRAS 19346+1209	IRAS 19454+2920
GY Aql	IRAS 19475+3119	IRAS 19500-1709	CRL 2477	RR Aql
CRL 2494	Z Cyg	IRC–10529	NSV 12961	IRC+80040
V Cyg	CRL 2646	IRAS 20541-6549	CRL 2686	CRL 2688
IRC+00499	UU Peg	CRL 5625S	IRAS 21373+4540	V460 Cyg
RT Cep	IRAS 21489+5301	IRAS 21554+6204	TW Peg	CRL 2901
IRAS 22272+5435	IRAS 22303+5950	CRL 3068	CRL 3099	IRAS 23268+6854
IRAS 23279+5336	IRC+40540	IRAS 23321+6545	RT Cep	
Stars which appeared to be extended, with a PSC CIRR2 flag > 4				
IRAS 05104+2055	RS Lib	χ Cyg	μ Cep	T Cep

IRAS numbers refer to the *IRAS* Point Source Catalog.

3. Results and Discussion

This list from which the stars were selected contained 283 stars. 4 of these stars fell within the small areas of the sky not covered by the *IRAS* survey. 65 of the stars were either near the galactic plane or confused with other sources, resulting in badly curved baselines. These stars were rejected. The data for the remaining 214 stars were processed by the MFP, and the calculations consumed more than 1 CPU year on a VAX 11/750 computer. 154 of the stars did not appear to be extended. 5 stars which did appear to be extended had a CIRR2 value greater than 4 in the PSC, suggesting the region may be contaminated by cirrus. These stars were also rejected. Table 1 list the stars that were rejected, along with those which were not found to be extended.

Figures 4 through 13 show the results of the MFP for the 54 stars that appeared extended in the 60μ data, and for IRC+10216 which appeared extended, but badly saturated the detectors. Three plots are shown for each star. The first plot shows the average of all the survey scans passing within 1' of the star's position. To produce this plot, the distance in the scan direction of the detector's center from the star's position was used to select the bin in which each data point would be averaged. There were 4 bins per arc minute. The second plot, labeled "DATA", shows this same average scan after the point source, fitted by the MFP, has been subtracted. The third plot, labeled "MODEL", shows a synthetic average scan. This plot was constructed by calculating the predicted flux from the extended portion of the model, at every point where data were actually measured. A bar is plotted under both the "DATA" and "MODEL" plots the length of which is the "diameter" of the CSS, defined as the geometric mean of the shell's major and minor axes.

3.1 Tests for Reliability of the Results

Several tests where performed to determine whether or not the extended emission reported by the MFP was real.

The first test was to run the MFP using data for sources that should not be resolved. Figure 14 shows the results of running the MFP on the 60μ data for 6 galaxies which were unresolved at all *IRAS* wavelengths (Soifer 1989). Except for the case of NGC 2966, the data for each of these galaxies is well approximated by the point source that the MFP fitted. In none of the galaxy test cases did the MFP fit a significant extended component.

Although the infrared cirrus emission was detected primarily at 100μ, it occasionally was seen at 60μ. If the area around the star being examined is contaminated by infrared cirrus emission, then the MFP might fit a dust shell to this emission even though it is not circumstellar in origin. A value greater than 4 for the PSC CIRR2 flag indicates the source is in a region which may be contaminated by cirrus emission. Figure 3A shows the CIRR2 flag distribution of all objects which the MFP reported were unresolved. The average CIRR2 value for this group is 3.6. Figure 3B shows the distribution for the objects which appeared to be resolved, including those with CIRR2 flags greater than 4. For this group, the average value is 2.6. On average, the objects which appear to be extended are in regions which are less apt to be contaminated with cirrus emission than are the unresolved objects, so it is

unlikely that the extended emission reported by the MFP was caused by infrared cirrus.

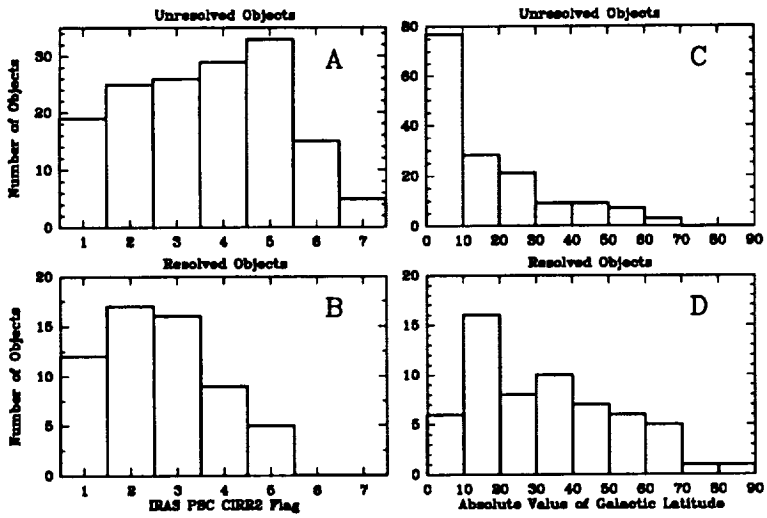

Fig. 3. A and B show the distributions of the PSC CIRR2 flag for the resolved and unresolved objects respectively. 154 objects were judged to be unresolved, however only 152 of these appear in the PSC (two failed to meet the strict confirmation criteria, even though individual *IRAS* observations show a strong detection). One resolved object, Y Hya, does not appear in the PSC and hence has no CIRR2 flag. C and D show the distribution of galactic latitudes among the unresolved and resolved objects. These two plots contain the objects which do not appear in the PSC.

Figures 3C and 3D show the distribution of absolute galactic latitudes, $|b^{II}|$, for the unresolved and resolved groups respectively. The unresolved objects are clustered nearer to the galactic plane than are the resolved ones, as one would expect if the resolved objects are less distant. The average $|b^{II}|$ value of the resolved group is 31.8°. If the resolved objects were distributed randomly about the sky, $|b^{II}|$ would average to 32.7°. This close agreement suggests that the average distance to the resolved objects is less than 1 kpc, the half thickness of the galactic disk. The greater clustering of the unresolved objects about the galactic plane explains the higher average CIRR2 value for that group.

As a final test, a function was defined to discriminate between cases where the MFP found significant amounts of extended emission, and those where it did not. The "Quality Function" is defined as

$$Q.F. = \frac{Q_0 F_{extended}}{F_{unresolved} R_{outer}^2}$$

where

$F_{extended}$ = The flux the model predicts from beyond 1' from the point source
$F_{unresolved}$ = The flux the model predicts from within 1 arc minute
R_{outer} = The geometric mean of the dust shell's semimajor and semiminor axes
Q_0 = The normalization constant

The ratio of the two fluxes in $Q.F.$ gives a measure of the fraction of the total flux arising from the resolved region of the CSS. The division by R_{outer}^2 is included to discriminate against model results predicting low intensity emission

from a very large area, which is apt to be caused by slight curvature in the scan baselines. The *Q.F.* function is normalized so that a spherical CSS with a radius of 5' and $F_{unresolved}/F_{extended} = 10$ will have a *Q.F.* value of 1. Values substantially less than 1 indicate the star is not resolved.

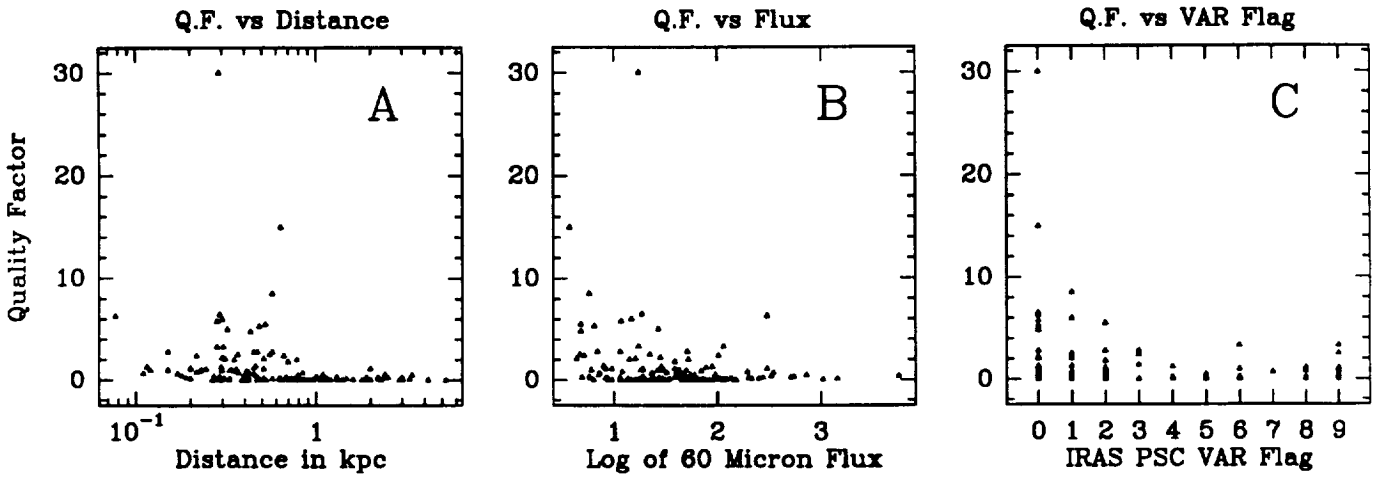

Fig. 17. The distribution of "Quality Factor" values as a function of distance, 60μ flux, and the *IRAS* PSC variability flag. Higher values of *Q.F.* correspond to sources that have been resolved. The *Q.F.* is shown for all 151 stars which were processed by the MFP and which have CIRR2 values of 4 or less. The average *Q.F.* value is 1.25, and many symbols overlap. Figure A does not include the stars IRAS 03074–8732, NSV 1835, NSV 12961 and IRAS 20541–6549, because no distance estimates were available for these stars. 35 of the stars shown in figure A are at distances of 1 kpc or more. The star at 2 kpc with a *Q.F.* greater than 1 is IRAS 05104 + 2055. This star is not included on the list of extended objects, because its CIRR2 flag is greater than 4. Figure C includes only the 55 stars which were judged to be extended.

Figure 17 shows the values of *Q.F.* for each star processed by the MFP, with a CIRR2 flag of 4 or less. In figure 17A, the *Q.F.* values are displayed as a function of the distance to the source. All of the large values of *Q.F.* come from objects less than 1 kpc away. This implies that the extended emission found by the MFP arises from a real shell around a nearby object, and is not a spurious feature of the data or the detector templates. Figure 17B shows the *Q.F.* values as a function of 60μ flux. Above average *Q.F.* values where obtained for sources differing by more than a factor of 1,000 in 60μ flux, therefore the extended emission is not just an artifact caused by the templates matching either very weak or very strong sources poorly. Most of the objects in figure 17B with 60μ flux values below 10.0 Jy have large *Q.F.* values. The average *Q.F.* value for these 20 objects is 2.8. To check whether some defect in the MFP caused all faint objects to have high *Q.F.* values, the data for 45 unresolved galaxies with flux values below 10 Jy were processed. The average *Q.F.* for these galaxies was 0.18, which is less than the *Q.F.* value for any of the objects we claim are resolved. Figure 17C shows the *Q.F.* values as a function of the PSC VAR flag, which gives the probability that a source is variable in the 12μ or 25μ bands. Above average *Q.F.* values are seen at all VAR flag values, so it is unlikely that source variability confused the MFP, and caused it to fit a spurious resolved component.

3.2 Results

Table 2 shows the model parameters for the 55 stars found to be extended in the 60μ data. While all stars with $Q.F. > 1.5$ are included in this table, stars with $Q.F. \approx 1$ were included only if the extended model appeared to fit the CRDD data appreciably better than a point source did. The fluxes quoted are not color corrected, and

were converted from the raw units of W m^{-2} to Janskys by assuming a flat energy spectrum $\nu F_\nu = 1$. The radii given in Table 2 are the geometric means of the major and minor axes of the best fit ellipsoidal shell.

3.2.1 100μ Results

At first glance, the 100μ data would seem to hold the most promise for detecting extended emission. The cool outer regions of the CSS should radiate most strongly around 100μ, even if the dust emissivity has a wavelength dependence as strong as λ^{-2}. In addition, the warm inner unresolved region will be relatively less dominant at 100μ than at 60μ. Unfortunately there are problems with the 100μ survey data that more than offset these advantages.

By far the worst problem with the 100μ data is the contamination of much of the sky by infrared cirrus. When the 100μ data for the 55 stars which were resolved in the 60μ data were examined, most of the scans were strongly curved, presumably due to infrared cirrus. In these cases even when the individual scans showed extended emission surrounding the star, it was impossible to find regions of the scan which were clearly free of emission and could be used to calculate the scan's baseline. The results of the MFP depend very strongly on the position of the scans' baselines, therefore if no baselines could be calculated, the scans could not be used. Only 16 of these 55 stars are in regions so free of cirrus emission that baselines could be calculated and the 100μ data could be processed with the MFP. In all cases except RY Dra all scans passing within 10' of the star's position were analysed. For RY Dra, all scans passing within 25' were used.

As an initial test, 100μ data for several unresolved galaxies were processed with the MFP. The MFP found almost all of them to be slightly resolved. This indicated that the 100μ detector response functions did not fit the survey data as well as the 60μ functions did. The cause of this is apt to be the fact that the 100μ data stream was passed through a 1.5 Hz low–pass filter (the filter for the 60μ data rolled off at 3 Hz). At the survey scan rate of 3.85' s^{-1}, this severe filtering significantly broadened the response to a point source beyond the 44" diffraction limit. The response functions were derived from pointed observations taken at 1/2 the survey scan rate, and therefore did not suffer as great a broadening. In order to compensate for this mis–match, the 100μ response functions were stretched in the in–scan direction until the MFP reported that the test galaxies were unresolved. The required stretch factor was 16%. Even after the response functions had been modified in this way, comparison of the CRDD data with simulated data produced with the response functions showed that the 100μ response functions did not fit the data as well as the 60μ functions did. For this reason only the stars with dramatically extended CSSs or very high signal/noise will be considered to have been resolved in the 100μ data. These stars are listed in table 2, and the MFP results are shown in figures 15 and 16.

All the stars found to be resolved in the 100μ band show a larger shell in the 100μ data than in the 60μ data. Since the model derived by the MFP is convolved with the detector response functions before it is compared with the data, the larger 100μ size is not an artifact of the telescope's poorer resolution at 100μ. It is likely that the size difference arises from a radial temperature gradient in the envelope. A similar systematic difference in the 60μ and 100μ sizes was found by Hawkins and Zuckerman (1991), who deconvolved the IRAS data for the strongest infrared planetary nebulae.

3.3 Physical Parameters

The angular size may be used to calculate the linear size of the CSS once the distance to the star is known. Table 3 lists the estimated distance and calculated envelope size for each star. The distance estimates were culled from the literature when available. Otherwise, the distances were estimated in one of the following three ways. For the nine Mira variables the Period-Luminosity-Spectral type relationship (Bowers and Hagen 1984) was used to calculate M_V, then m_V was used along with an estimate of the extinction, to calculate the distance. This technique was analysed by Celis (1980), who estimated the mean error in the derived distance is 19%. Semi-regular variable stars were assumed to all have $M_K = -6.7$ (Kleinmann 1989). The m_K was obtained from the 2μ survey, and the distance was calculated ignoring extinction. All other stars were assumed to have a luminosity of $10^4 L_\odot$, and the

spectral type was used to calculate M_K.

If it weren't for the interstellar medium, the age of each CSS could easily be calculated from its size and the expansion velocity obtained from CO observations. The ISM should appreciably slow the expanding envelope once the density of the expanding shell has decreased to equal the density of the ISM. If the star's envelope is expanding at 15 km $s^{-1}$and the mass loss rate is $10^{-6}M_{\odot}yr^{-1}$, equal density will occur at a shell radius of 0.3 pc, assuming an ISM density of 1 H cm^{-3}. The envelope will have expanded to this size after only 2×10^4 years, which is much shorter than the period of time that any star remains on the AGB. Therefore the effect of the ISM on the shell size cannot be ignored.

Table 2.
Model Results for Stars Found to be Extended

60μ Results									
Name	R_{outer} (arcmin)	R_{inner} (arcmin)	F_{ps} (Jy)	F_{ext} (Jy)	Name	R_{outer} (arcmin)	R_{inner} (arcmin)	F_{ps} (Jy)	F_{ext} (Jy)
R Scl	6.5	1.1	60.4	6.1	RY Dra	18.9	1.9	8.8	6.9
CRL 278	5.1	0.7	45.3	5.5	RT Vir	4.1	1.0	40.7	6.3
o Cet [F]	2.2	0.0	287.0	89.1	SW Vir	11.4	0.5	57.4	12.2
V Eri [A]	8.0	2.8	25.5	5.4	R Hya	5.7	1.8	106.4	21.4
ST Cam	3.1	0.5	7.1	2.0	W Hya	10.5	0.7	216.2	76.5
R Lep	4.8	0.4	28.8	2.7	RX Boo	6.6	0.5	75.9	12.1
W Ori	6.2	2.1	15.8	5.9	X Tra [C]	4.1	1.3	15.4	9.2
R Aur	4.0	0.1	24.7	5.7	X Her	6.2	0.0	43.9	5.7
W Pic	6.4	1.0	5.6	2.6	NGC 6720 [E]	5.4	0.1	55.1	13.7
α Ori [F]	10.5	0.2	302.9	165.2	V1942 Sgr [A]	3.2	0.2	2.7	3.2
U Ori [C]	6.7	1.3	43.1	8.9	UX Dra	4.0	0.2	5.0	2.1
UU Aur [C]	4.3	0.5	18.2	11.8	AQ Sgr [B]	3.0	1.2	6.0	3.4
NGC 2346	6.3	1.5	8.4	2.2	R Cyg [G]	4.8	2.0	13.5	3.6
Y Lyn [C]	4.2	1.4	12.2	3.1	V1943 Sgr	5.0	0.9	29.7	7.7
X Cnc	8.9	1.2	7.6	1.2	X Pav	4.9	0.7	54.7	8.9
RS Cnc	5.8	1.0	36.7	4.0	RT Cap	8.1	1.0	5.1	3.1
R Leo	3.8	0.8	127.0	29.0	T Ind	2.9	0.8	5.1	0.6
IRC+10216 [D,F]	6.6	0.0	6048.3	441.9	Y Pav [B]	5.8	0.6	7.2	3.0
Y Hya	9.7	1.3	8.3	3.6	S Cep	3.9	0.9	32.2	3.2
CIT 6 [F]	7.0	0.4	300.4	13.8	RV Cyg [A]	6.0	1.5	12.1	6.0
U Ant [A]	4.7	0.6	28.6	15.4	EP Aqr	5.9	1.5	55.1	5.8
U Hya [A]	2.9	1.3	12.5	48.3	PQ Cep [C]	7.3	2.1	10.1	2.6
VY UMa [B]	3.1	0.1	4.4	1.7	SV Peg	4.7	1.5	26.9	1.2
R Crt	5.9	1.9	59.5	9.2	π Gru	4.9	0.6	89.4	11.3
IRC–30163	6.8	2.3	33.9	7.1	V PsA	5.1	1.2	19.8	2.4
BK Vir	5.6	1.5	21.0	3.1	TX Psc	3.1	0.1	11.8	4.5
Y UMa	3.8	1.7	16.4	2.9	R Cas [C]	4.3	1.0	116.5	27.0
Y CVn [B]	5.5	2.8	19.0	10.7					
100μ Results									
Name	R_{outer} (arcmin)	R_{inner} (arcmin)	F_{ps} (Jy)	F_{ext} (Jy)	Name	R_{outer} (arcmin)	R_{inner} (arcmin)	F_{ps} (Jy)	F_{ext} (Jy)
V Eri [A]	8.9	1.0	5.6	7.5	RY Dra	22.1	5.3	4.4	31.1
W Pic	18.4	4.1	3.6	23.8	SW Vir	15.0	4.7	15.4	23.5
IRC+10216	9.5	0.7	865.8	256.0	W Hya	15.0	2.4	72.0	65.1
Y CVn [B]	6.3	1.2	5.9	11.0	RX Boo	12.6	4.8	25.1	16.6

[A]These objects are listed as extended at 60μ and 100μ in the *IRAS* Small Scale Structure Catalog

[B]These objects are listed as extended at 60μ in the *IRAS* Small Scale Structure Catalog

[C]These objects are listed as extended at 100μ in the *IRAS* Small Scale Structure Catalog

[D]IRC+10216 saturated the 60μ detector and produced strong optical cross–talk in the 60μ band. The windows used to fit a baseline before processing were not free of these effects, and the 60μ results given by the MFP are probably spurious. The 100μ data are largely free of these effects.

[E]NGC 6720 is listed as extended at 12μ and 25μ in the *IRAS* Small Scale Structure Catalog

[F]These values were obtained from fits to the small data set provided by the default ADDSCAN search radius of 1.7'. The data obtained using 10' search radius were not used, because they showed signs of optical cross–talk.

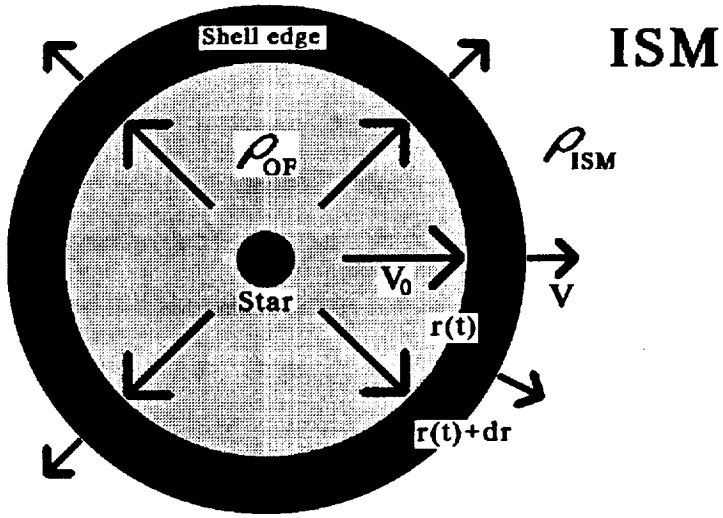

Fig. 18. A dust shell expanding into the ISM. The leading edge of the expanding shell is slowed as it sweeps up material from the ISM. The edge is prevented from slowing to a halt by the pressure of the material behind it, which is still moving at the original speed of v_0.

The mean free path for scattering against hydrogen atoms even at a low ISM density of 1 H cm^{-3} is only $\sim 10^{-3}$ pc, so we can assume that the interaction between the ISM and the stellar wind occurs very near the edge of the expanding shell. The shell loses speed as it expands into the ISM and must accelerate the ambient material. Once the outer edge has been slowed by the ISM it will be pushed by material behind it which is still expanding at the original outflow speed.

The rate at which the outer edge expands can easily be calculated. Let p be the total momentum of the expanding envelope edge, moving with a speed of v and having mass m (see figure 18).

$$F = \frac{dp}{dt} = v\frac{dm}{dt} + m\frac{dv}{dt} \qquad (1)$$

The material behind the shell edge is still moving with its original expansion velocity v_0, and it exerts a force on the shell edge of

$$F = 4\pi r^2 v_0 \rho_{OF}(v_0 - v)$$

where r is the shell's outer radius. This force acts to maintain the velocity of the expanding shell. During a short time interval of length dt, the shell edge gains material of mass

$$dm = 4\pi r^2 \rho_{OF}(v_0 - v)dt + 4\pi r^2 \rho_{ISM} v dt \qquad (2)$$

The first term in dm accounts for the stellar wind colliding with the edge from behind, and the second term accounts for the mass of ISM material that is swept up. If the mass loss rate $\dot{M}$ and outflow speed v_0 are assumed to be constant then

$$\rho_{OF} = \frac{\dot{M}}{4\pi r^2 v_0} \qquad (3)$$

With these assumptions equation (2) can be integrated to give the total mass of the shell edge

$$m = 4\pi \int_0^t r^2(\rho_{OF}(v_o - \frac{dr}{dt}) + \rho_{ISM}\frac{dr}{dt})dt = \dot{M}(t - r/v_0) + \frac{4}{3}\pi r^3 \rho_{ISM} \qquad (4)$$

Substituting equations (2) and (4) into equation (1) gives

$$4\pi r^2 v_0 \rho_{OF}(v_0 - v) = 4\pi r^2(\rho_{OF}(v_0 - \frac{dr}{dt}) + \rho_{ISM}\frac{dr}{dt})\frac{dr}{dt} + (\dot{M}(t - r/v_0) + \frac{4}{3}\pi r^3 \rho_{ISM})\frac{d^2r}{dt^2}$$

The above equation can be solved for $d^2r/dt^2 = dv/dt$, yielding equations (5a&b), a system of two coupled differential equations which can be solved to give the shell's radius as a function of time.

$$\frac{dr}{dt} = v \qquad (5a)$$

$$\frac{dv}{dt} = \frac{\dot{M}(v_0 - v) - (\dot{M}(1 - v/v_0) + 4\pi r^2 \rho_{ISM})v}{\dot{M}(t - r/v_0) + \frac{4}{3}\pi r^3 \rho_{ISM}} \qquad (5b)$$

Table 3. — Shell Sizes, Ages and Masses

(1) Name	(2) Distance (pc)	(3) Source for Distance	(4) Radius (pc)	(5) V_0 (km s^{-1})	(6) $\dot{M}$ ($10^{-7} M_\odot yr^{-1}$)	(7) Source for V_0 and $\dot{M}$	(8) Age (10^3 yr)	(9) Mass ($M_\odot$)	(10) Spectral Type
R Scl	400	1	0.76	24.7	73.0	4	32	0.23	CII
CRL 278	230	7	0.34	7.6	4.2	12	59	0.025	M7III
o Cet [A,B]	77	2	0.05	5.0	1.7	4	10	0.002	M5.5e
V Eri	370	7	0.86	13.0	4.2	12	94	0.039	M5/M6IV
ST Cam	480	3	0.43	10.0	1.8	3	64	0.012	N
R Lep	410	1	0.57	20.5	21.0	4	33	0.069	CIIe
W Ori	340	3	0.63	11.8	1.8	3	98	0.018	CII
R Aur [A]	366	4	0.42	10.9	10.0	4	50	0.050	M7III
W Pic	660	1	1.23	7.0	1.1	1	280	0.031	N
α Ori [B]	200	4	0.61	15.0	11.0	4	66	0.072	M2I
U Ori [A]	244	5	0.48	7.5	2.7	16	110	0.030	M6.5e
UU Aur	290	3	0.36	13.4	4.0	6	39	0.016	CII
NGC 2346	460	6	0.84	19.0	100.0	6	57	0.57	C envelope
Y Lyn	570	9	0.69	5.4	0.48	9 [C]	210	0.010	M5Ib-II
X Cnc	460	3	1.19	12.0	2.2	3	170	0.037	CII
RS Cnc	410	4	0.69	5.3	6.3	4	150	0.092	M6IIIase
R Leo [A]	304	4	0.33	4.0	2.6	4	93	0.024	M8IIIe
Y Hya	510	1	1.44	10.2	2.3	1	290	0.066	C
CIT 6 [B]	190	4	0.39	16.9	23.0	4	40	0.091	C envelope
U Ant	320	1	0.43	21.2	8.7	1	29	0.025	N
U Hya	290	1	0.24	7.9	1.9	1	36	0.007	CII
VY UMa	520	3	0.46	8.4	1.1	3	65	0.007	CII
R Crt	120	10	0.20	11.0	0.17	12 [C]	39	0.001	M7III
IRC–30163	300	15	0.59	8.0	0.36	12 [C]	190	0.007	O envelope
BK Vir	150	10	0.24	4.7	0.036	13 [C]	120	0.0004	M7III
Y UMa	310	7	0.34	6.5	1.3	7	61	0.008	M7II-III
Y CVn	280	3	0.45	9.0	1.3	3	64	0.008	CIab
RY Dra	450	3	2.48	10.0	2.1	3	470	0.098	C
RT Vir [A]	697	4	0.82	11.3	29.0	4	73	0.21	M8III
SW Vir	180	7	0.60	9.4	3.2	7	91	0.029	M7III
R Hya [A]	115	5	0.19	7.5	0.053	9 [C]	64	0.0003	M7IIIe
W Hya	216	5	0.66	9.7	0.33	9 [C]	200	0.007	M8e
RX Boo	230	4	0.43	11.5	7.1	4	43	0.031	M7.5
X Tra	300	1	0.36	9.2	1.4	1	66	0.009	C
X Her	450	9	0.81	8.5	1.2	9 [C]	130	0.016	M8
NGC 6720 [D]	780	17	1.23	24.0	—	18	—	—	—
V1942 Sgr	630	1	0.59	10.0	1.7	1	100	0.017	CII
UX Dra	430	3	0.50	6.9	1.5	3	100	0.015	CII
AQ Sgr	570	1	0.50	6.0	1.8	7	120	0.021	CII
R Cyg [A,B]	420	6	0.59	11.3	4.6	6	80	0.037	S
V1943 Sgr	300	8	0.43	8.0	1.9	7	78	0.015	M7III
X Pav	150	19	0.21	10.5	0.75	20	32	0.002	M
RT Cap	510	1	1.21	9.1	1.0	1	280	0.028	CII
T Ind	550	1	0.46	5.5	0.8	1	98	0.008	CII
Y Pav	450	1	0.75	9.4	1.8	1	110	0.021	CII
S Cep [A]	296	5	0.33	22.4	1.6	12 [C]	26	0.004	CII
RV Cyg	470	3	0.82	14.7	5.2	3	110	0.055	CII
EP Aqr	110	10	0.19	8.6	0.18	12 [C]	43	0.001	M8III
PQ Cep	360	10	0.76	21.7	4.2	14 [C]	70	0.030	C
SV Peg	170	10	0.23	11.0	0.57	12 [C]	38	0.002	M
π Gru	200	8	0.28	14.9	13.0	7	21	0.028	S
V PsA	330	8	0.49	21.0	6.9	7	28	0.019	M7III
TX Psc	280	1	0.25	12.1	2.7	1	24	0.007	CII
R Cas [A]	216	4	0.27	12.3	8.6	4	28	0.024	M7IIIe

[A] These sources are Mira variables

[B] These results are from processing the small data set provided by the default ADDSCAN parameters. All others used the data set obtained by changing the ADDSCAN search radius to 10'.

[C] The mass loss rates for these objects were calculated from the CO(1-0) or CO(2-1) line strengths and widths, using formula 9a or 9b from van der Veen and Rugers, 1989

[D] Much of the molecular envelope of NGC 6720 has been dissociated by the central star, therefore observations of CO cannot be used to determine the precursor star's mass loss rate.

Sources — (1) Olofsson *et al* 1988. (2) Allen 1973. (3) Olofsson *et al* 1987. (4) Knapp *et al* 1985. (5) Using P-L-S relationship from Bowers and Hagen 1984. (6) Knapp *et al* 1986. (7) Knapp unpublished. (8) Knapp *et al* 19??. (9) Wannier P.G. and Sahai, R. 1986. (10) Assuming an absolute K magnitude of -6.7 (Kleinmann 1989). (11) Assuming a luminosity of $10^4 L_\odot$. (12) Zuckerman and Dyck 1986. (13) Zuckerman and Dyck 1988. (14) Zuckerman *et al* 1986. (15) van der Veen and Rugers 1989. (16) An unpublished CO(3-2) spectrum taken at the CSO was used, along with an LVG radiative transfer program (Morris 1980). (17) Huggins and Healy, 1986. (18) Leene and Pottasch 1988. (19) See text. (20) Deguchi *et al* 1990 (these authors assume a distance of 300 pc for X Pav, $\dot{M}$ has been rescaled here for a distance of 150 pc).

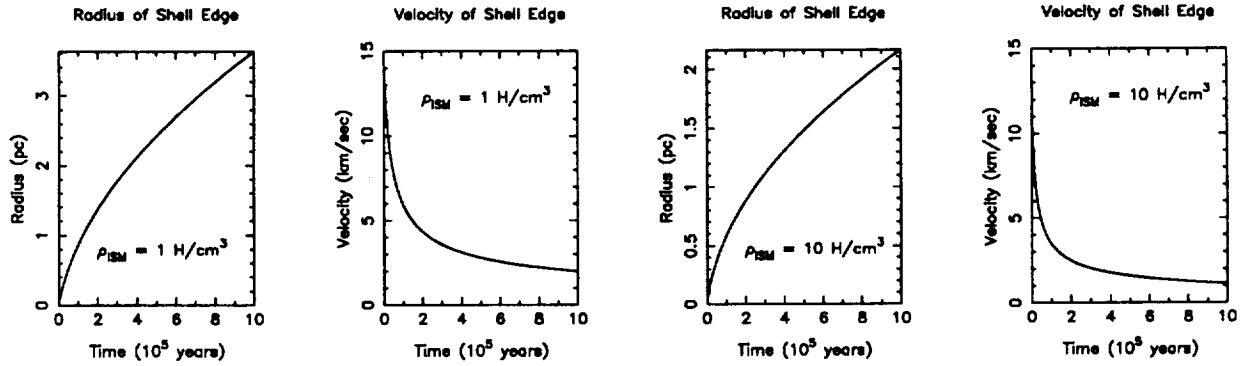

Fig. 19.

The results of numerically integrating equations 5a and 5b are shown for two values of the ISM density ρ_{ISM}. In both cases $\dot{M} = 10^{-6} M_\odot \mathrm{yr}^{-1}$ and $v_0 = 15$ km s^{-1}. The period of copious mass loss for an AGB star probably lasts for $\sim 5 \times 10^5$ years, and over that period the expansion velocity of the shell edge drops from 15 km s^{-1} to under 3 km s^{-1}. This deceleration would be difficult to detect from molecular line observations. The CO envelope is truncated at a radius of 0.1 pc or less, even for very large mass loss rates (Truong-Bach *et al.* 1990). If the CSS has expanded beyond the dissociation radius, then the molecular emission lines won't show signs of deceleration because the molecular material will only be present in a region where the ISM has already been swept away. On the other hand, if the CSS has not yet expanded to the dissociation radius, the shell is so small that the velocity of the shell edge will not yet have been significantly reduced.

Equations (5a&b) were numerically integrated to solve for the age of each star found to be extended. For consistency, the CSS radius from the 60μ data was used in all cases, even if a 100μ was available. The results are given in table 3. The ISM density was assumed to fall off exponentially, in the direction z perpendicular to the galactic plane, from a value of 2 H cm^{-3} (Spitzer 1978), with a scale height of 100 pc (Mihalas and Binney 1981). The mass loss rates were taken from calculations in the literature. The dust was assumed to have been

ejected from the star at the terminal velocity derived from the CO profile. The velocity difference between the dust and the gas (the "drift velocity") was ignored. The drift velocity is probably small for optically thick shells with $\dot{M} \geq 2 \times 10^{-5} M_{\odot} \mathrm{yr}^{-1}$ (Gail and Sedlmayr 1985), while calculations for the drift velocity in optically thin shells (Berruyer and Frish 1983, Goldreich and Scoville 1976) predict drift velocities larger than the terminal velocity for the molecular material. However it is unlikely that the drift velocity can greatly exceed 20 km s^{-1}, because beyond that velocity the grains will be destroyed by sputtering (Kwok 1975). Ignoring the drift velocity results in an over–estimate of the shell's age. As figure 19 shows, the expansion rate of the shell edge is not strongly dependent upon ρ_{ISM}; the final size of the shell is reduced by less than a factor of 2 when ρ_{ISM} is increased by a factor of 10.

The Mira variables in table 3 are of particular interest. Since Miras obey a period-luminosity relationship, their distances can be estimated much more accurately than is possible for the other objects in the table. The average age of the shells around the Miras is 6.0×10^4 years. This suggests that the duration of the period during which Mira variables are losing detectable amounts of mass is about 10^5 years. The Mira variable with the youngest shell, 10^4 years old, is Mira itself. U Ori's shell is 1.1×10^5 years old, the oldest of any of the Miras. The average CO outflow velocity for the Mira in table 3 is 10.2 km s^{-1}. This is higher than the average outflow velocity of all Miras which have been detected in CO (Young *et al.* 1992) which is 6.8 km s^{-1}(σ = 2.7 km s^{-1}). This suggests that either the Miras with low outflow velocities have smaller dust shells which were not resolved by *IRAS*, or that the extended dust shells surrounding these low velocity Miras contained too little material to be detected. The second explanation is more likely, because radiative transfer models of the CO emission from these stars suggests that the mass loss rate correlates strongly with the outflow velocity (Knapp *et al.* 1982, Young *et al.* 1992).

The average radius of the shells in table 3 is 0.59 pc. Since this table consists only of those stars which appear to have been resolved, stars with large shells are over-represented. The shells surrounding V Eri (fig. 4D), W Ori (fig. 5A), W Pic (fig. 5C), Y Hya (fig. 7A), RY Dra (fig. 8E), RT Vir (fig. 8F), W Hya (fig. 9C), X Her (fig. 9F), RV Cyg (fig. 11E) and PQ Cep (fig. 12A) are at least twice as large as the maximum size of 0.3 pc predicted by Rowan-Robinson (1986). The mass loss rates and ages from table 3 show no correlation.

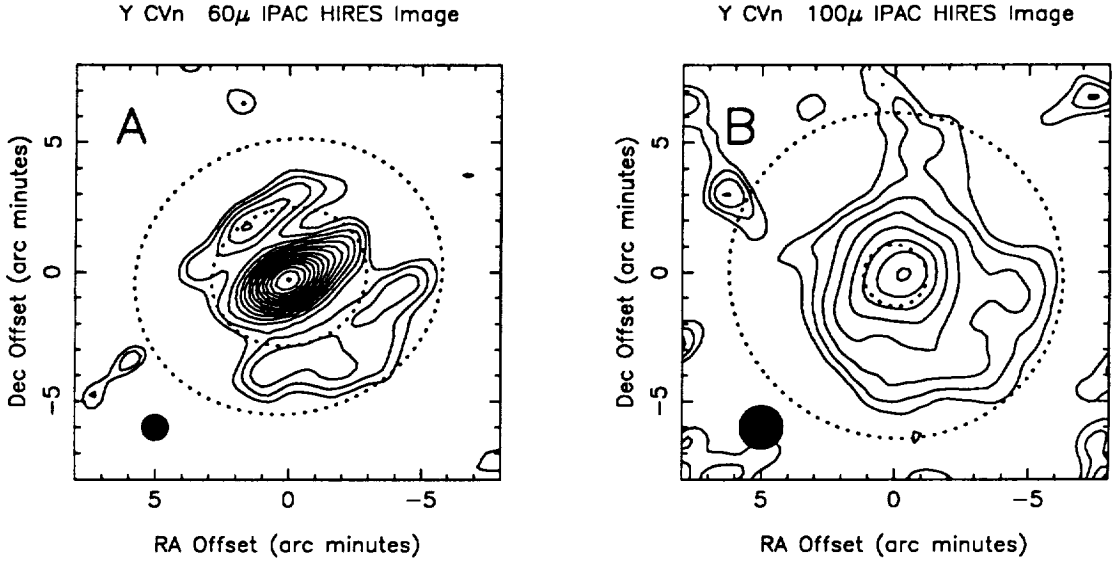

Fig. 20. The results of processing the survey data covering Y CVn with the IPAC HIRES program suite are shown. In figure A, the 60μ map, the lowest contour level is 0.45% of the peak intensity, and the contours are logarithmically spaced with ratios of 1.5. The central source appears elongated, however this is almost certainly an artifact caused by the large size of the 60μ detectors in the cross–scan direction. Figure B shows the 100μ HIRES map. Here the lowest contour is 2% of peak intensity, and the ratio between successive contours is 1.7. In both figures the inner and outer extents of the dust model fitted by the MFP are shown as dotted lines. The filled circles show the *IRAS* resolution (80% encircled energy).

3.4 Detached Shells

One of the parameters fitted by the MFP was the inner radius of the CSS. These radii are listed in Table 2, and several of them are larger than the 1' resolution of *IRAS* at 60μ. In particular, the shells surrounding V Eri, W Ori, R Crt, IRC-30163, Y UMa, Y CVn, RY Dra, R Hya, R Hya and PQ Cep have inner radii larger than 1.5'. These stars may have entered a quiescent period of reduced mass loss. Figure 20 shows the 60μ and 100μ maps produced by analysing the survey data for Y CVn with the IPAC HIRES processor (Aumann *et al.* 1990). While the HIRES image shows that the CSS has a more complex structure than the simple dust model used by the MFP, the outer edge of the MFP model dust shell matches the maximum extent of emission in the map quite well. The MFP calculated an inner radius of 2.8' for the 60μ data, and the map also shows a similar inner radius for the extended emission. However the 1.2' inner radius derived from the 100μ data is nearly equal to the resolution of *IRAS* at 100μ, and probably has no physical significance.

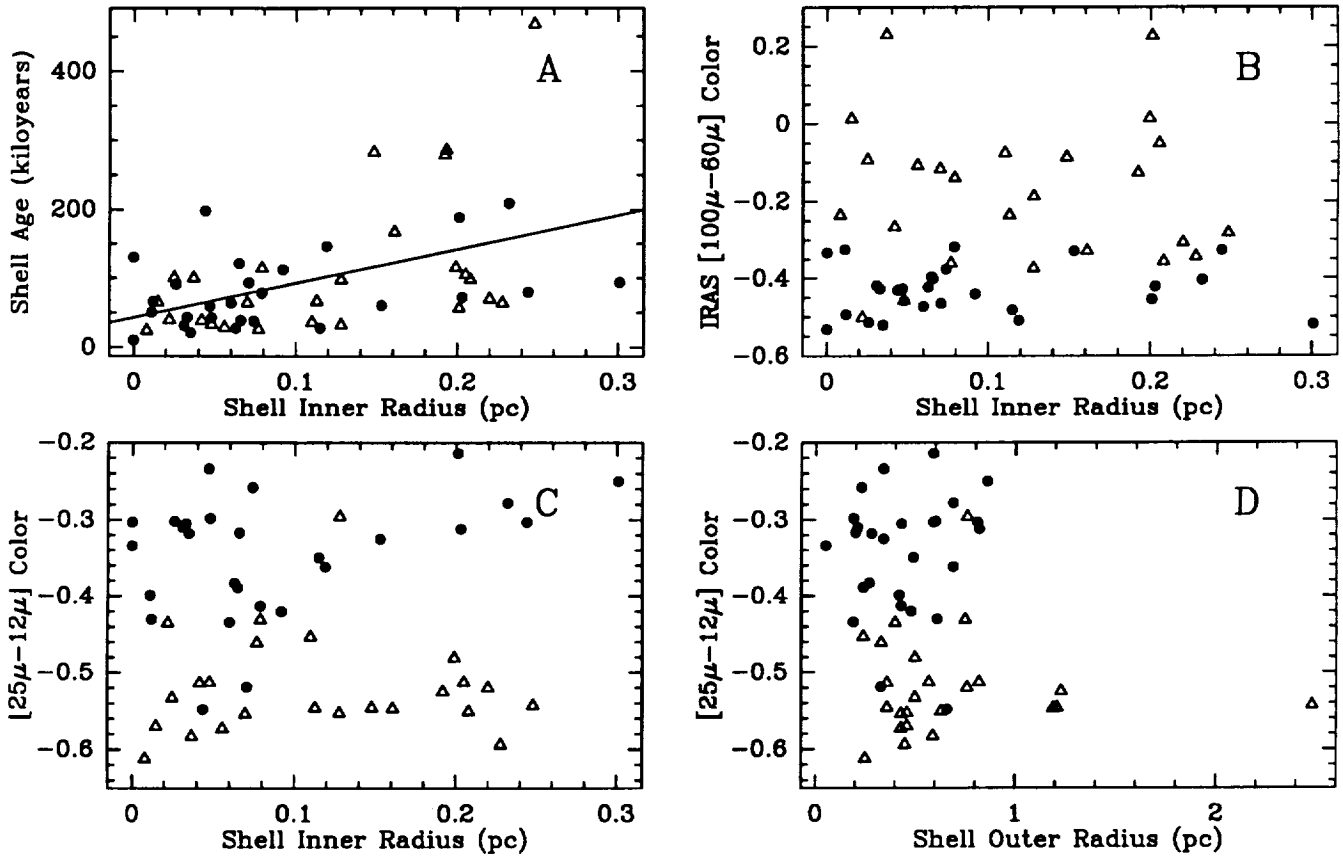

Fig. 21. Oxygen rich stars are plotted as filled circles and carbon stars are plotted as open triangles. (A) – The calculated age of the dust shells for 53 of the stars in table 3, plotted as a function of the inner shell radius. Also shown is the least-squares best fit line. NGC 6720 was not included in this plot, because its age was not calculated. The weak correlation is stronger for the carbon rich envelopes. (B, C & D) – IRAS Colors from the PSC plotted as a function of inner and outer

shell radius. Y Hya does not appear in the PSC, and is not shown in these three plots. NGC 2346 and NGC 6720 are not plotted in figures C and D.

Figure 21A shows the age of 53 of the dusts shells from table 3, plotted as a function of the inner shell radius in parsecs. These two quantities appear to be weakly correlated. The linear correlation constant, r, for these two variables is 0.47. The probability of r having this high a value if the age and inner shell radius are uncorrelated is less than 0.001 (Young 1962). However since the age of the shell is strongly correlated with its *outer* radius (r = 0.86), a spurious correlation could occur between the age and the inner radius. This would happen if the assumed dust emission profile, or the MFP itself had a defect which caused shells with large outer radii to be fitted with large inner radii. Since the outer radii must be larger than the inner radii, the two radii will be correlated even if the MFP is not defective, and this tautologous correlation could give rise to an age – inner radius correlation.

Figures 21B&C show that there is no correlation between the infrared color of the object, and the shell's inner radius. This is surprising if the calculated inner radii are correct, since one would expect a detached shell to be cooler, allowing the star's photosphere to dominate the 12μ and 25μ bands. Figure 21D shows that the 4 largest shells surrounding stars still on the AGB have $[25\mu - 12\mu]$ colors roughly consistent with photospheric emission, implying that these envelopes may be detached. These 4 shells, which also have large inner radii, surround the carbon stars W Pic, X Cnc, Y Hya and RT Cap. However the best candidate for a detached shell is the S star χ Cygni (see section 3.7).

If the weak correlation of age with inner radius is not spurious it suggests that the mass loss process becomes more episodic as the star loses its atmosphere. For AGB stars, this might occur as a consequence of the thermal pulse cycle. Throughout the thermal pulse phase, the amplitude of the luminosity variation caused by a thermal pulse increases with each successive pulse (Iben and Renzini 1983). Since it is likely that the stellar winds from these stars are driven by radiation pressure, these luminosity variations could modulate the mass loss rate, and produce shells which appear to be detached from the central star.

3.5 Comparison of Resolved and Unresolved Objects

As figure 17 shows, a large fraction of the stars with distances of 500 pc or less appear to be resolved. While all 8 of the stars with distances less than 200 pc are resolved in the 60μ data, there are 29 stars within 500 pc which are not. These stars are listed, along with their estimated distances and CO outflow velocities, in table 4. Using Kleinmann's (1989) scale heights of 200 pc for carbon stars and 400 pc for oxygen–rich stars, the total number of stars in our CO selected list (both resolved and unresolved) as a function of distance is well fit by an exponential disk, out to a distance of 350 pc. The best fit space densities are 120 kpc^{-3} for carbon stars and 230 kpc^{-3} for oxygen–rich stars. Beyond 350 pc our list must be quite incomplete because the number of stars per unit distance drops off rapidly. The fact that the list of resolved stars in table 3 contains nearly equal numbers of carbon and oxygen–rich objects, even though the oxygen–rich stars are twice as common, is a reflection of the larger average size of the carbon star shells.

The average distance to the unresolved stars is 375 pc. At that distance a CSS with a radius $\geq$ 0.2 pc could be clearly resolved. This is 1/3 the average CSS size of the resolved stars listed in table 3. Therefore if the distance estimates for the unresolved stars are not too low by a factor of 2 or more, their shells must either be much smaller on average than those of the resolved stars, or not dense enough to be detected by IRAS. If the unresolved stars have shells which are just as large as those of the resolved stars, but less dense, then either the mass loss rates for these stars must be lower, or the outflow velocity must be higher. However the average CO velocity for both the unresolved and resolved groups (excluding the resolved stars with distances greater than 500 pc) is 12 km s^{-1}. Since the mass loss rate is correlated with the expansion velocity (Knapp *et al.* 1982, Young *et al.* 1992), it is likely that the mass loss rates of these two groups are also similar. Therefore the unresolved stars should not have less dense envelopes, implying that they must have smaller envelopes than the resolved stars. Since the average expansion velocities agree closely, the CSSs surrounding the unresolved stars must also be younger.

Table 4. – Stars Within 500 pc Which Are Unresolved

Name	Distance (pc)	V_0 (km s^{-1})	Name	Distance (pc)	V_0 (km s^{-1})	Name	Distance (pc)	V_0 (km s^{-1})
R And	310	8.7	W Cnc	470	4.3	RU Her	410	9.2
W And	470	11.0	CRL 5254	420	12.8	U Her	360	11.6
IRC−30023	470	11.6	IRAS 09371+1212	500	25.0	g Her	200	10.0
R Hor	270	6.6	R LMi	400	6.0	IRC+10365	500	16.7
TW Hor	420	5.3	V Hya	330	20.0	RS CrA	280	20.7
NML Tau	270	22.0	S Vir	290	3.5	W Aql	470	19.9
TX Cam	330	16.9	CRL 4211	330	20.5	RR Aql	420	7.4
V Cam	390	12.2	S CrB	310	7.8	IRC+80040	480	12.0
S CMi	340	4.1	IRAS 15194−5115	400	23.3	CRL 3099	500	10.1
R Cnc	300	3.4	R Ser	260	5.6			

A color–color diagram for these nearby unresolved stars, along with all the stars found to be resolved, is shown in figure 22. While the stars found to be resolved are divided nearly evenly between carbon stars (26 objects) and oxygen–rich (M) stars (27 objects), only 6 of the 29 unresolved nearby stars are carbon stars. This suggests that the carbon stars have been losing mass for a longer time, on average, than have the M stars. The calculated shell ages in table 3 provide additional evidence of this. The average age of the carbon star shells is 1.10×10^5 yr, whereas the average age of the oxygen–rich shells is 8.1×10^4 yr.

Because most of the carbon stars within 500 pc which were processed are resolved (19 out of 25, ignoring IRC+10216), the ages of these stars can be used to estimate the duration of the carbon star phase of evolution for stars in the solar neighborhood. The average age for these stars from table 3 is 8.6×10^4 yr. If we assume that these stars are, one average, half way through the carbon star phase then the implied duration of this phase is about 1.5×10^5 yr. This is almost an order of magnitude longer than the lifetime of 2×10^4 yr calculated by Willems and de Jong (1988). Even if the interaction of the CSS with the ISM is ignored, and the age is calculated by simply dividing the CSS size by the molecular expansion velocity, and the unresolved stars are assumed to have an age of 0 yr, the average age is 4.0×10^4 yr, implying a carbon star lifetime of 8×10^4 yr. One potential source of error in this calculation is that the molecular velocity has been used, rather than the unknown dust expansion velocity. However the dust velocity would have to be at least 4 times as large as the molecular velocity, requiring an average drift velocity of ≥ 60 km s^{-}1 to force the lifetime calculated here to match that of Willems and de Jong. A drift velocity this large will result in grain sputtering, and also implies a dust density which is too low to produce the flux detected by *IRAS* at a reasonable temperature (see section 3.7).

Not surprisingly, the resolved stars have redder $[100\mu - 60\mu]$ colors on average than do the unresolved objects. None of the stars with $[100\mu - 60\mu] < -0.54$ were resolved, and all of the stars with $[100\mu - 60\mu] > -0.37$ (including NGC 6720 and NGC 2346 which are not shown in figure 22) were resolved. However the extended stars have *bluer* $[25\mu - 12\mu]$ colors than the nearby unresolved stars. All of the objects with $[25\mu - 12\mu] < -0.475$

were found to be extended.

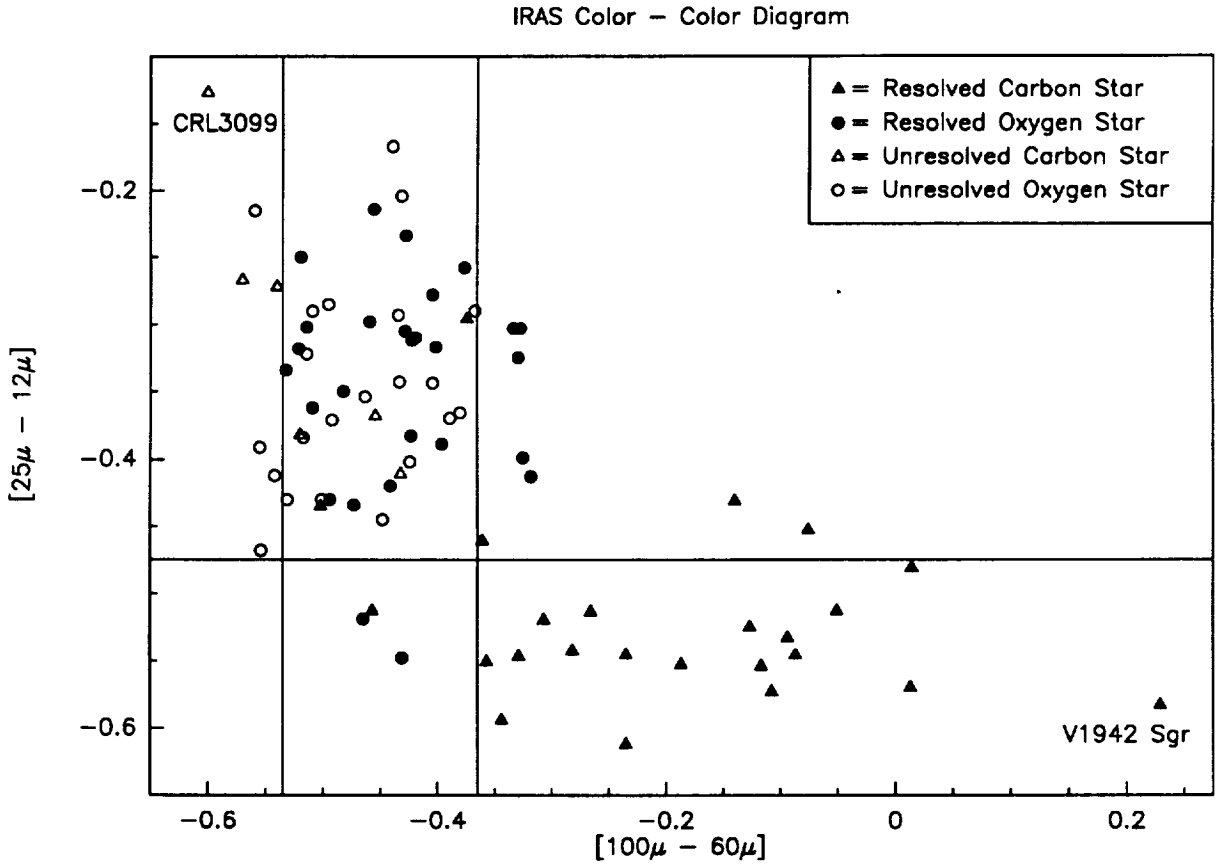

Fig. 22. An *IRAS* two color diagram is shown for all extended objects (filled symbols) and for objects within 500 pc which were not found by the MFP to be extended (open symbols). No color corrections have been applied to the fluxes from the PSC. Not shown are two planetary nebulae with very blue [25-12] colors, NGC 6720 and NGC 2346. IRAS 09372+1212 is not shown because it was not detected by *IRAS* at 12μ, Y Hya is not shown because it does not appear in the PSC.

3.6 The Interaction of the Shells with the ISM

The resolved stars are all less distant than 1 kpc, and most are within 500 pc. Being this nearby, most of these objects have measurable proper motions. The proper motion can be combined with the radial velocity from the CO observations, to calculate the full three dimensional velocity of the star ($\vec{v}_{\rm LSR}$) with respect to the local standard of rest. Borkowski and Sarazin (1990) have found that the envelopes of planetary nebulae with large velocities relative to the local ISM are often distorted by the ISM ram pressure. While the simple model fitted by the MFP does not include this effect, the model is ellipsoidal. Distortion caused by the ISM might increase the eccentricity of the fitted shell. Any distortion should be most easily seen in larger shells which, for a given $\dot{M}$ and v_0, will have less

dense outer edges more easily deformed by the ISM ram pressure. However no correlation was found between the eccentricity of the shell and the shell size. Because ram pressure increases quadratically with the star's velocity with respect to the ISM, and since this velocity will nearly equal $\vec{v}_{LSR}$ in the solar neighborhood, the shells of stars which large $|\vec{v}_{LSR}|$ should be the most distorted, but once again no such correlation is seen. The shells of stars near the galactic plane are not any more eccentric than those located far from the plane, where the ISM density should be less. Finally, there is no correlation between $\dot{M}$ and the eccentricity. We therefore find no evidence in this study that the shape of the CSS is distorted as a result of ram pressure from the surrounding ISM.

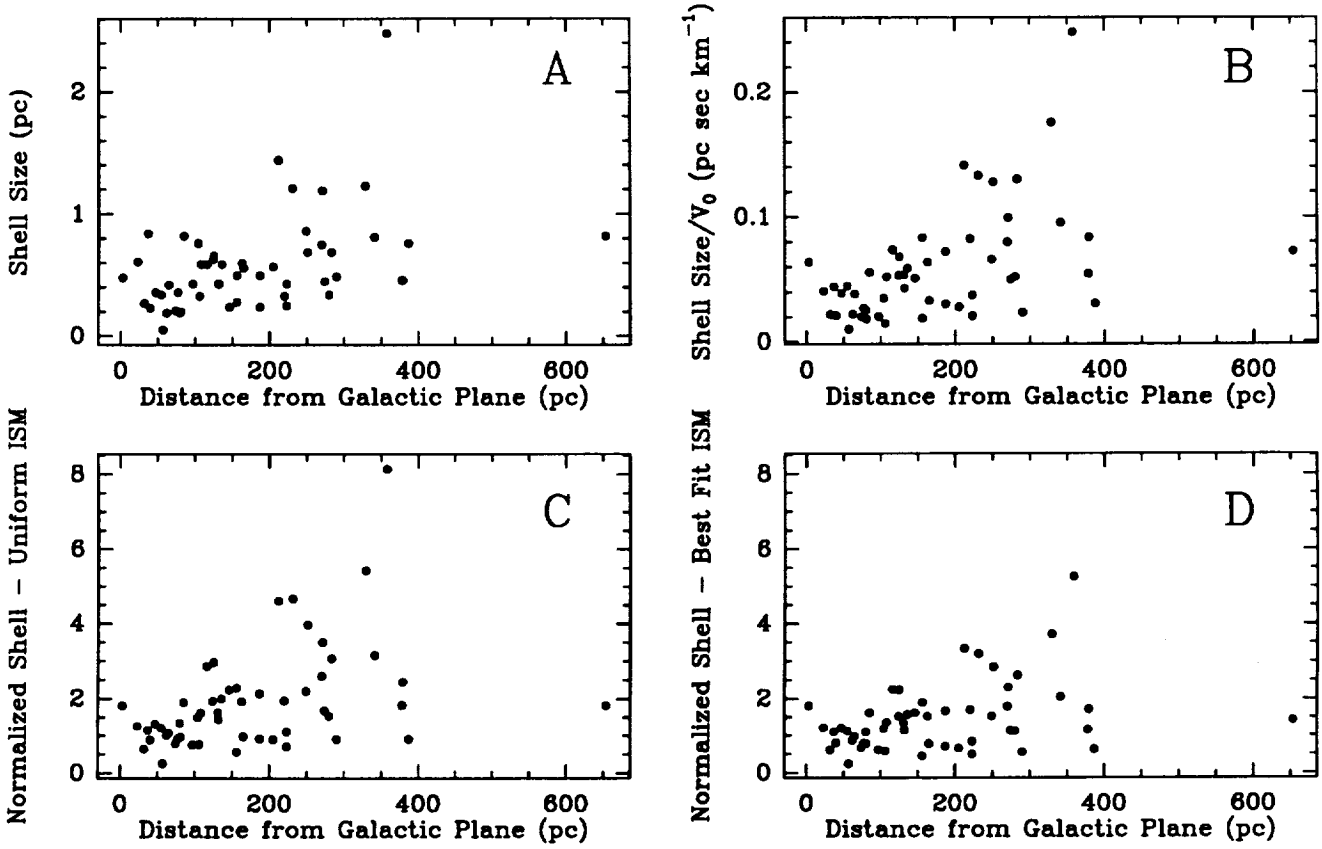

Fig. 23. (A) The distribution of shell sizes as a function of the object's distance from the galactic plane (z). There is a weak correlation between these two quantities which is improved by dividing the shell size by the expansion velocity as shown in (B). The correlation is still visible when the shell size is normalized by the size expected for a star with the averaged age, located in a uniform ISM (C). Reducing the ISM density exponentially as z is increased reduces the correlation (D). The scale height which minimizes the correlation is 70 pc.

The size of a star's shell (S) does appear to be affected by the ISM. Figure 23A shows that the shells surrounding stars far from the galactic plane are larger on average. The linear correlation coefficient between S and $|z|$ is 0.43, which indicates correlation with a confidence level above 99.8%. One would not expect the correlation to be perfect because parameters unrelated to the ISM density, such as the shell age and expansion velocity, also

effect the size of the shell. A shell expelled at a high velocity will, for a given age and $\dot{M}$, be larger than one expelled at a low velocity. The S, $|z|$ correlation does not arise from this effect, because there is no correlation between v_0 and $|z|$. However normalizing S by v_0 improves the S, $|z|$ correlation slightly, as shown in figure 23B.

The average age for a shell near the galactic plane ($|z| \leq 100$pc) is 6×10^4 yr. Figure 23C shows the size of each shell divided by the size it would have if it had been expanding into a uniform ISM with $\rho_{ISM} = 2$ H cm^{-3}, for 6×10^4 yr. As expected, this normalized shell size has an average value of 1 for shells near the galactic plane. However the average normalized shell size for stars with $|z| \geq 200$pc is 2.7. These high $|z|$ shells are bigger than the shells near the galactic plane either because they are older, or because the shells near the galactic plane have been truncated through interactions with the ISM, or because the ISM at high z has a lower density, and allows the shells to expand more freely.

If the S, $|z|$ correlation is caused by the drop off of ISM density with increasing $|z|$, then it can be used to calculate the ISM z scale–height. As figure 24 shows, the expansion model represented by equations 5a&b predicts that shell size should increase logarithmically with decreasing ISM density, over the density range $10^{-1} < \rho_{ISM} < 10^{1}$. If the ISM density drops off exponentially with increasing $|z|$, then S and $|z|$ should have a linear correlation. The scale–height of the ISM, H_{ISM} can be calculated as follows. Calculate normalized shell sizes N by dividing the actual shell sizes by model shells calculated using each star's $\dot{M}$, V_0 and $|z|$. Assume in the model calculations that $\rho_{ISM} \propto exp(-h|z|)$. The best estimate for H_{ISM} is the reciprocal of the value of h which minimizes the linear

correlation between N and $|z|$. For the data shown in figure 23 the best estimate is H_{ISM} = 70 pc.

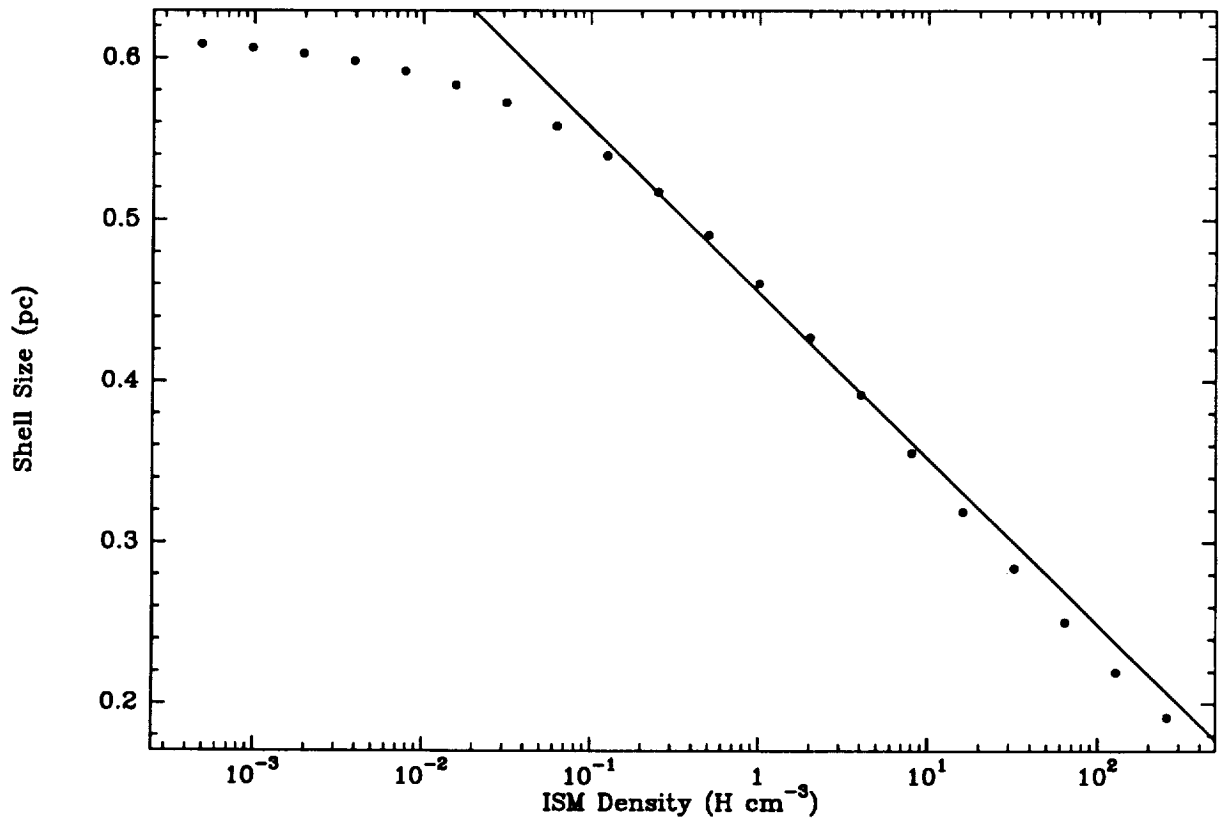

Fig. 24. The expected shell size is shown as a function of ISM density. The star was assumed to be expelling $10^{-6}\dot{M}_{\odot}$ of material per year with an initial velocity of 10 km sec^{-1} for a period of 6×10^4 years. The line shown is the least–squares best fit for the density range 10^{-1} to 10^{1} hydrogen atoms per cm^3.

3.7 The Dust Temperature

The estimated shell masses from table 3 can be combined with the extended emission flux values from table 2, to calculate mean temperatures for the resolved region of the dust shells. Hildebrand (1983) showed that for spherical dust grains

$$M_{\rm shell} = \frac{F(\nu)D^2}{B(\nu,T)} \frac{4/3a\rho}{Q(\nu)} \left[\frac{M_{\rm gas}}{M_{\rm dust}}\right] \qquad (6)$$

where

M_{shell} = the mass of the resolved portion of the dust shell
$F(\nu)$ = the 60μ flux from the resolved region
D = the distance to the star
$B(\nu, T)$ = the Planck function at frequency ν and temperature T
a = the radius of a dust grain.
ρ = the density of the dust material, assumed here to be 3 gm cm^{-3}
$Q(\nu)$ = the emissivity of the dust at frequency ν
$[M_{gas}/M_{dust}]$ = the gas to dust mass ratio, assumed here to be 100

An iterative procedure was used to find a temperature which satisfied equation 6, for each shell except that of NGC 6720, for which no mass loss rate was available. The mass of the material within a radius of 1' was subtracted from the mass listed in table 3 to produce an estimate of the mass of the resolved region. The dust grains where assumed to have radii of 0.1μ, and an emissivity of 0.0046 was used. This emissivity was obtained by interpolating values tabulated by Draine (1987). The emissivities of graphite spheres and spheres of "astronomical silicate" differ negligibly at 60μ. The 60μ flux values from table 2 where multiplied by 1.03, to color correct them for a 40 K black body.

Figure 25A shows a histogram of the temperatures calculated by solving equation 6. The average temperature is 36 K. The average outer radius for these shells is 0.58 pc. Collison and Fix (1991) modeled the temperature profiles of axisymmetric circumstellar dust shells by solving the radiative transfer problem. They found that all temperature profiles exhibited the same basic shape

$$T(r) = T_0\left(\frac{r_0}{r}\right)^{0.4} e^{-\xi(1-r_0/r)} \approx T_0\left(\frac{r_0}{r}\right)^{0.4} e^{-\xi} \qquad (r \gg r_0) \qquad (7)$$

where r_0 is the radius at which dust condenses with a temperature of T_0, and ξ ranges from 0.48 near the pole to 0.86 near the equator of their model shells. Equation 7 implies that the temperature at large r is not strongly dependent upon r, so the average temperature of 36 K obtained by solving equation 6 should be a good estimate of the temperature at 1/2 the average outer radius (0.29 pc). This temperature is in fair agreement with the value of 30 K obtained from equation 7 with T_0 = 1000 K, r_0 = 50 AU, ξ = 0.67 (the average of the polar and equatorial

values) and $r = 0.29$ pc.

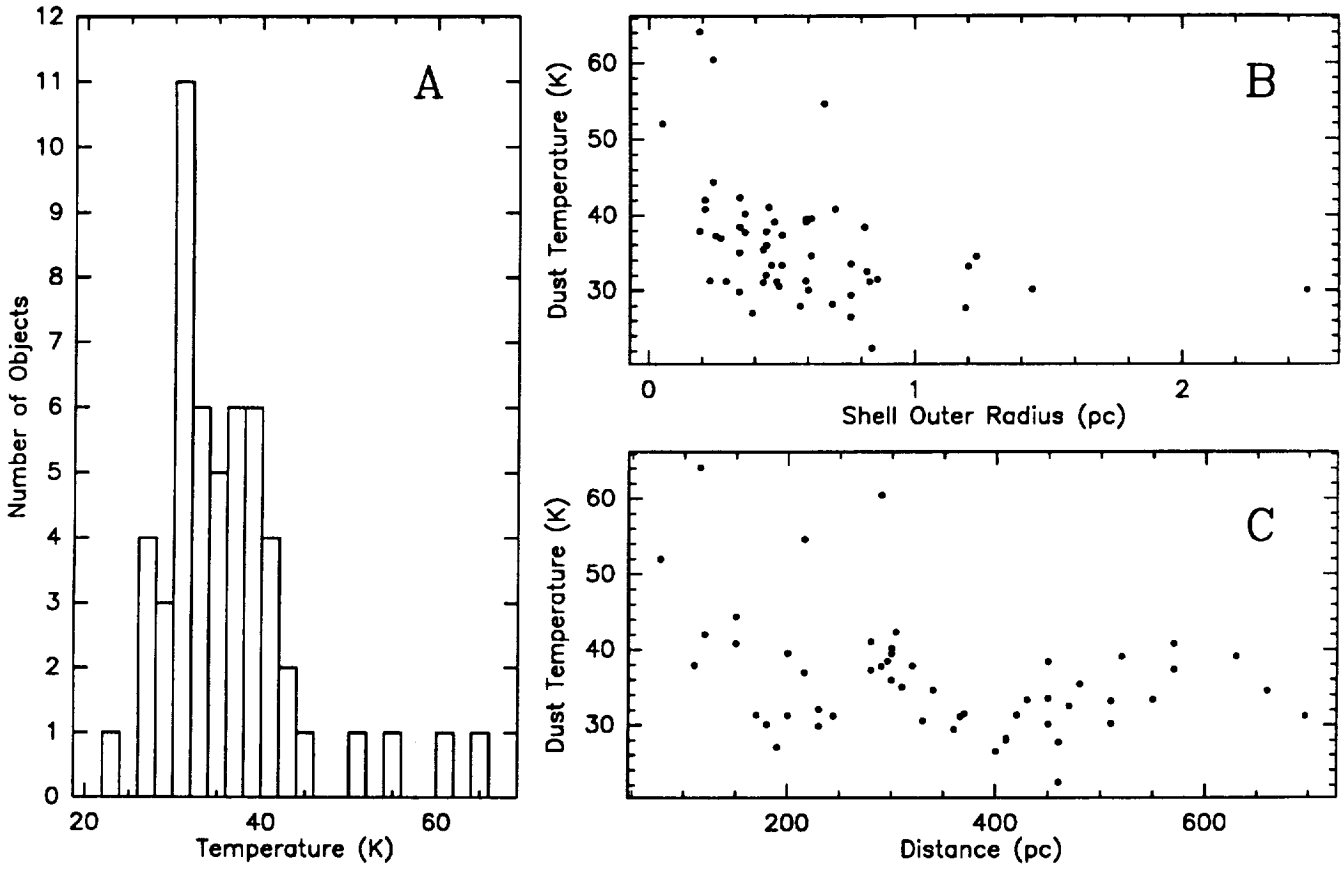

Fig. 25. Figure A shows a histogram of calculated dust temperatures. Four of the shells, those of o Cet (52 K), W Hya (55 K), U Hya (60 K) and R Hya (64 K) seem to be significantly warmer than average. B shows the distribution of calculated shell temperatures as a function of the shells' outer radii. Note that with one exception the warmest shells are much smaller than average, therefore the average temperature of the dust should be higher. C shows the calculated shell temperatures as a function of distance. All of the warmest shells are closer than average, allowing material nearer the star to be resolved.

Figure 26 shows the radial dependence of $I_{60\mu}/I_{100\mu}$ for the stars which were found to be extended in the 100μ data. IRC+10216 was not included, because of the low reliability of its 60μ model parameters. This ratio decreases for all the stars from a radius of 0.1 pc to a radius $\approx$ 0.5 pc. Assuming there is no radial gradient in the grain emissivity, this decrease must arise from a decrease in dust temperature. The dust within this region must be heated either by radiation from the central star, or by collisions with the expelled gas. The data become progressively more noisy as the edges of the envelopes is approached, but the four stars (V Eri, W Pic, RY Dra, and W Hya) with the largest envelopes show that $I_{60\mu}/I_{100\mu}$ stops decreasing at a radius of about 0.9 pc. The nearly constant ratio beyond 0.9 pc indicates that in the outer envelope the dust is externally heated.

These temperature gradient regimes have been noted separately in earlier work. Hawkins (1990) presented

IRAS 60μ and 100μ maps of R Hya obtained from the same survey data used here, and also found it to be extended in both bands. The maps show the CSS has a radius of 15' – 20'. This is in fair agreement with the 10' 60μ and 15' 100μ sizes for this object listed in table 2, obtained from the MFP. Hawkins compared the 60μ and 100μ data, and derived a dust temperature of $\sim$ 40 K in the outer envelope, in good agreement with the average temperature of 36 K obtained by solving equation 6. He found that $I_{60\mu}/I_{100\mu}$ decreases radially and showed that this is consistent with radiative heating of the dust by W Hya. Though not remarked upon by the author, the Hawkins data also indicate $I_{60\mu}/I_{100\mu}$ no longer decreases beyond a radius of 0.9 pc (assuming the distance used here, 216 pc, rather than 115 pc used by Hawkins). Gillet *et al.* (1986) present *IRAS* pointed observations of R CrB. For this object $I_{60\mu}/I_{100\mu}$ is constant across the entire 18' diameter shell, excluding an unresolved central hot–spot which covers the inner 1 pc radius of the shell (using the author's distance of 1.6 kpc). The dust temperature inferred by the authors is 25K–30K. Both of these earlier works, plus the results in figure 26, indicate that within the central 0.5 pc the dust is heated primarily by the central stars' radiation, while an external heat source dominates beyond about 1 pc.

Gillet *et al.* (1986) developed a model for the radial temperature profile and infrared brightness of an envelope heated by both its central star and an external heat source the effects of which are constant throughout the envelope. This model was used to produce the three curves shown in figure 26. The three curves represent the expected value of $I_{60\mu}/I_{100\mu}$ for stars of $10^4 L_\odot$(upper curve), $5 \times 10^3 L_\odot$, and $3 \times 10^3 L_\odot$(lowest curve). In all three cases the central star was assumed to emit as a 2500 K black body, the dust emissivity $\sim \lambda^{-1}$, and the external heating rate equals that of a $10^4 L_\odot$ star at a radius of 0.9 pc. Models with dust emissivity $\sim \lambda^{-2}$ were also calculated, however the value of $I_{60\mu}/I_{100\mu}$ at radii > 1 pc were much too high, even with no external heat source.

In section 3.5 it was shown that our results suggest that the carbon star phase of evolution lasts substantially longer than the lifetime estimate of Willems and de Jong (1988). One way in which our results could be brought into agreement with those of Willems and de Jong is by assuming that the dust has a substantially larger terminal velocity than the molecular material. This is by no means excluded by the results of some of the models of dust acceleration which can be found in the literature. For example Wickramasinghe (1972) calculated that the dust should typically be accelerated to a terminal velocity of several thousand km s^{-1}! However if the dust is expanding at a much higher velocity than the molecular material, then equation 3 tells us that the density of the dust in the CSS must be less than the molecular expansion velocity and the dust/gas ratio near the star would suggest. This means that we must obtain the far infrared fluxes measured by *IRAS* from a much smaller total amount of solid material. If we assume the dust velocity is five times that of the CO (the minimum increase required to make our carbon star age estimates consistent with Willems and de Jong's lifetime estimate), then equation 6 must be solved with a correspondingly smaller effective dust/gas ratio. This increases the average estimated dust temperature from 36K to 49K, which does not agree as well with the 30K predicted by equation 7, or the temperatures implied by

$I_{60\mu}/I_{100\mu}$.

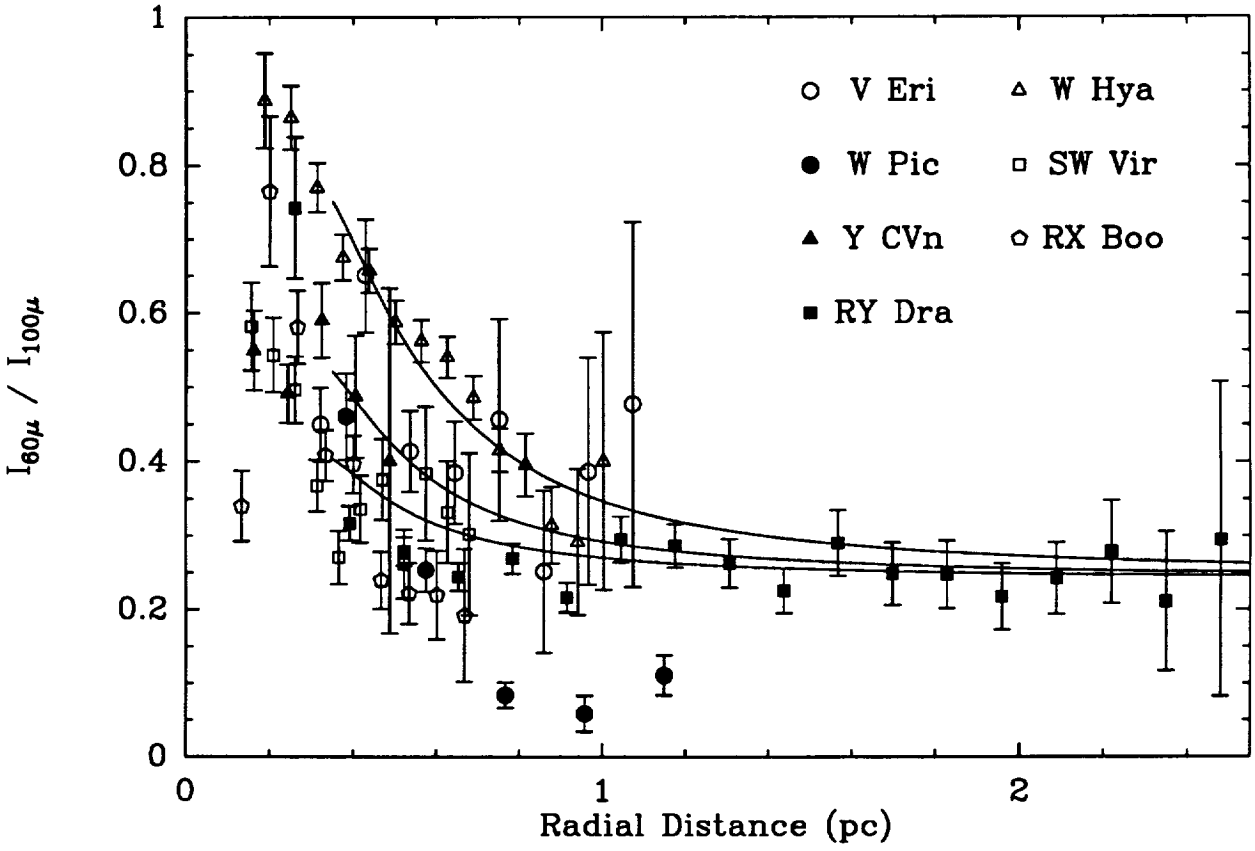

Fig. 26.

The radial dependence of the ratio of the 60μ and 100μ brightness is shown for the stars which are extended in the 100μ data. In this figure, the raw CRDD data have been summed after baseline removal in 1' wide annular bins of increasing radial distance from the central star. Filled symbols, for W Pic, Y CVn and RY Dra, represent carbon star data. Data at radii $< 2'$ are not shown. Several points from radii less than 0.3 pc with $I_{60\mu}/I_{100\mu} > 1.0$ are not shown. The error bars represent the value of

$$\sigma(60\mu/100\mu) \equiv \left(\frac{1}{I_{100\mu}}\right)\sqrt{\frac{\sigma^2_{60\mu}}{N_{60\mu}} + \frac{I^2_{60\mu}\sigma^2_{100\mu}}{I^2_{100\mu}N_{100\mu}}}$$

where $\sigma_{60\mu}$ and $\sigma_{100\mu}$ are the standard deviations in $I_{60\mu}$ and $I_{100\mu}$, and $N_{60\mu}$ and $N_{100\mu}$ are the numbers of points in the annular bins. For clarity of the figure, the very substantial error bars for the abscissa are not shown.

3.8 Notes on Particular Objects

W Pictoris: The 18.4' radius of the 100μ emission surrounding this star (figure 15B) is the largest of any of the CSSs presented here, corresponding to 3.5 pc (assuming a distance of 660 pc). The 60μ emission (figure 5C) covers a much smaller area, however no well defined outer edge is seen in the 60μ emission, suggesting noise may be obscuring emission from beyond a radius of $\sim 7'$. The size of the 100μ envelope is so large, it is questionable whether the extended emission is actually associated with the star. The extended emission at both 60μ and 100μ is well centered on the star's position, and the MFP reported the emission arises from a a nearly circular region with an aspect ratio of 0.96 in both bands. The object is at a fairly high galactic latitude ($b^{II} = -31$), however its PSC CIRR2 flag is 4, indicating the field may be contaminated by infrared cirrus. The CIRR1 flag, which is a count of the objects within 30' which were detected by *IRAS* only in the 100μ band and are apt to be cirrus structures, is 0. A search of the SIMBAD and NED databases revealed no objects within 20' of W Pic which could produce the 100μ emission.

Assuming the 100μ emission is is circumstellar in origin, the mass loss rate and outflow velocities derived from CO observations (Olofsson *et al.* 1988) imply that near the outer edge the CSS has a density of only 4×10^{-3} H cm^{-3}. Even at this star's distance of 330 pc above the galactic plane, the surrounding ISM should be dense enough that the CSS would require more than 10^6 years to expand to 3.5 pc. It therefore seems likely that in order for the CSS to reach this size, either W Pic must lie in a region of very low ISM density, or its mass loss rate must have been much greater in the past.

RY Draconis: This object is surrounded by the second most extensive region of emission of all those examined. If the extended emission is circumstellar, the radius is 2.9 pc (assuming a distance of 450 pc). As with W Pic, the size is so large, it is possible that the extended emission arises from a chance alignment with an object not associated with the star. RY Dra has a high galactic latitude ($b^{II} = 51°$), so it is unlikely that this region is contaminated by infrared cirrus. Also, the PSC CIRR1 and CIRR2 flags are 0 and 3 respectively, indicating the region is relatively free of cirrus contamination. A search of the SIMBAD and NED databases revealed only two cataloged objects within 20' of RY Dra; SAO 15949, a 10th magnitude F2 star 9' away and IRAS F12532+6600, a faint galaxy 17' away who's 60μ flux is 2.5 mJy, and which was undetected at 100μ. Neither of these objects could be responsible for the extended emission around RY Dra.

RY Dra differs from W Pic in that the size and shapes of the 60μ and 100μ regions are very similar (see figures 8E and 15E). Throughout most of the extended emission, $I_{60\mu}/I_{100\mu} \approx 0.25$ which is near the middle of the range for infrared cirrus clouds (Low *et al.* 1984). If the extended emission is circumstellar in origin, the temperature of the dust shell is nearly constant throughout the outer envelope. As with W Pic, the CO–derived mass loss rate and outflow velocity (Olofsson *et al.* 1987) imply a very low density near the outer edge of the CSS, again indicating that either the surrounding ISM has a very low density, or the star's mass loss rate was greater in the past.

NGC 6720 (the Ring Nebula): Hawkins and Zuckerman (1991 here after HZ) also analysed the survey data for this object, by performing an one dimensional deconvolution. The results they obtained differ significantly from those presented here. The 60μ diameter they obtained is 50", far smaller than the 10' diameter we obtained. The source of this disagreement is shown in figure 27A&B. The HZ diameter is a Full Width at Half Maximum, whereas the MFP reports a size at zero intensity. Since the extended emission is very weak, it has very little effect on the FWHM. However HZ examined the individual detector scans in an attempt to find low level emission which might

arise from a weak infrared halo, and found none.

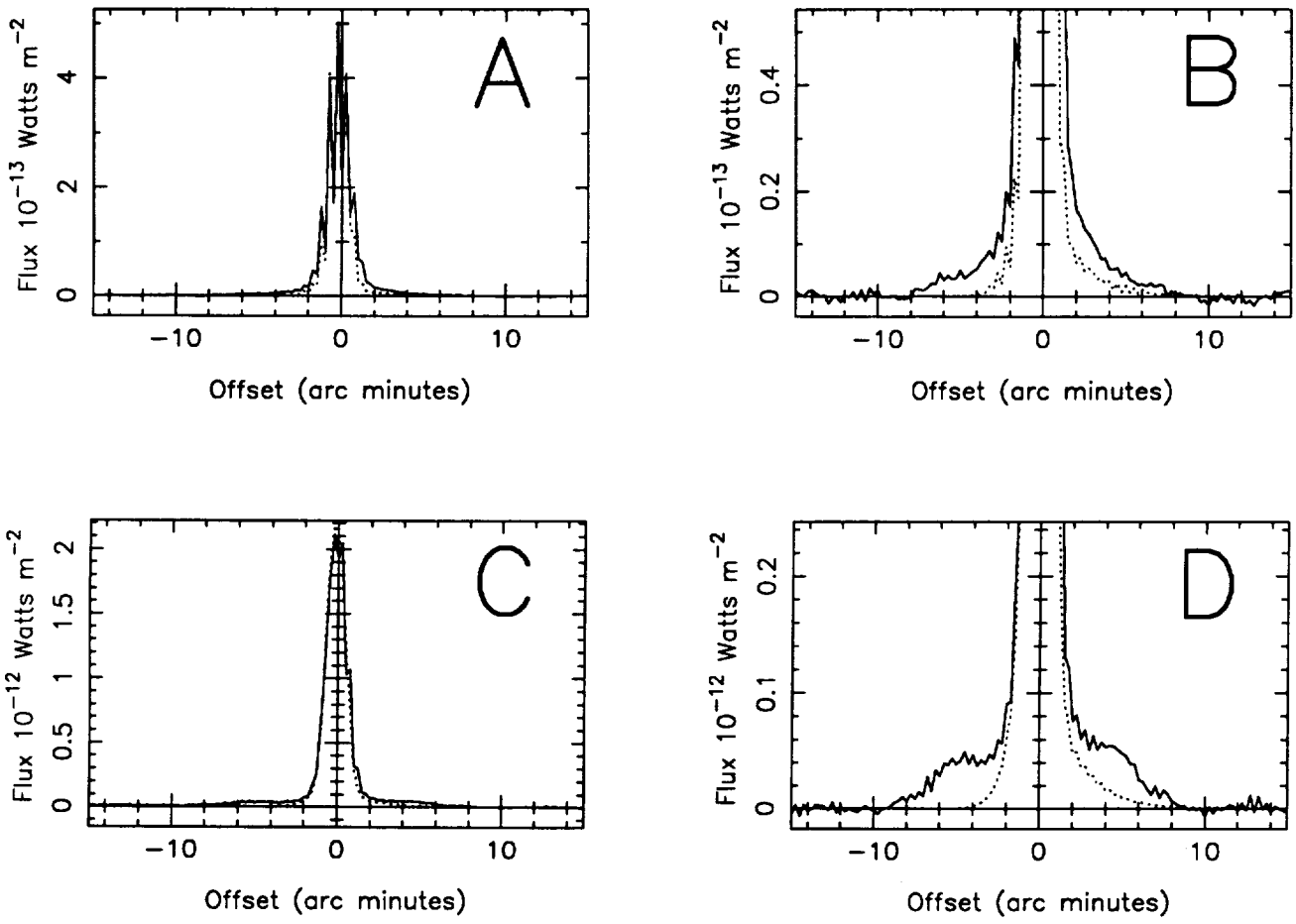

Fig. 27. (A) The solid line shows the 60μ data for NGC 6720, binned as in Fig. 1. The dotted line shows the best–fit point source for these data. (B) The same data show in A, but with an expanded vertical scale. Note that emission is seen several arc minutes further from the source than can be explained by the detector's point spread function alone. (C) shows the binned data for χ Cygni (solid line) and the best–fit point source (dotted line). The extended emission region is very flat, suggesting the CSS is hollow. (D) is the same data as in C plotted with an expanded vertical scale.

χ Cygni: This object is not listed in tables 2 and 3, because its PSC CIRR2 flag is 5, suggesting that the field may be contaminated by infrared cirrus. Nevertheless, this object does appear to be extended (see figure 27C&D), and the 60μ survey scans covering the object have reasonably flat baselines. Unfortunately the 100μ scans show abundant evidence of cirrus contamination. The 60μ shell has a radius of 7', and it is strikingly flat-topped, suggesting the shell is detached, with an inner radius of 3.5'. If a distance of 140 pc (obtained using the Bowers and Hagen P-L-S relationship) is adopted, the inner and outer radii are 0.14 and 0.29 pc respectively, and the shell age obtained by solving equations (5a&b) is 3.4×10^4 years. Further evidence that χ Cygni has a detached shell is provided by its *IRAS* [12-25] and [25-60] colors, which correspond to a temperature of 2000–2500 K. This indicates most of the infrared radiation from this star arises from the star's photosphere. This is in sharp contrast to the situation for most of the AGB stars with detectable molecular emission, the colors of which usually indicate

the presence of dust at a temperature below 1000 K. Had this star not been rejected due to its CIRR2 flag (which is only 1 unit above the rejection threshold), it would have been the best example of a detached shell in the entire sample. χ Cygni is not listed in the *IRAS* small scale structure catalog.

4. Conclusions

The *IRAS* survey data for 279 red giant stars which have been detected in rotational transitions of CO were processed using a simple model fitting program. This program was developed to detect the presence of low intensity extended emission surrounding a bright unresolved source. 55 of these stars were found to have shells which are resolved in the *IRAS* 60μ data. The average shell radius is 0.59 pc. These 55 stars are about equally divided between carbon stars and stars which oxygen–rich envelopes. A model for the interaction of the expanding shell with the surrounding ISM was developed. This model predicts that the edges of the largest shells (those with radii > 1 pc) will be expanding at much lower speeds than the inner envelope, where the CO emission arises. From examining the resolved envelopes we conclude that:

1) The average age for the shells surrounding the 9 Mira–type stars which are extended is 6×10^4 yr. This suggests that the period during which these stars lose mass lasts for $\sim 10^5$ yr. The oldest shell found surrounds U Ori, and the youngest surrounds Mira itself.

2) Some shells appear to be detached from the central star. This phenomenon is more common among older stars, suggesting that the mass loss process becomes more episodic as the star sheds its envelope. This might be caused by the the star's thermal pulse cycle, which has an increasingly pronounced effect on the stellar atmosphere as the envelope mass decreases.

3) Although all 8 stars less distant than 200 pc are resolved in the *IRAS* 60μ data, 29 stars within 500 pc were not. These stars probably have younger CSSs than those which were resolved.

4) Almost all the carbon stars with distances of 500 pc or less have resolved shells, while only 1/2 of the oxygen–rich stars do. The resolved carbon star shells also are older on average than the oxygen–rich ones. These facts imply that carbon stars have been losing mass for a longer period, on average, than oxygen–rich red giants. The average age of these nearby carbon stars is 8.6×10^4 yr, which indicates the lifetime of an average carbon star is 1.5×10^5 yr.

5) Large CSSs tend to be found at large distances from the galactic plane, confirming that the ISM density limits the size to which a CSS can grow. Surprisingly, even very large shells seem to be nearly spherical, and do not appear to be distorted by ram–pressure caused by the star's motion with respect to the ISM.

6) Radiative transfer models and the value of $I_{60\mu}/I_{100\mu}$ allow the average dust temperature in the outer regions of a CSS to be estimated. The typical value obtained is about 35 K. This provides a constraint on the value of the dust drift velocity, because a very large drift velocity results in a low dust density in the outer shell which in turn requires a high dust temperature to produce the 60μ and 100μ fluxes measured by *IRAS*. The radial dependence of $I_{60\mu}/I_{100\mu}$ suggests that an external heat source supplies most of the thermal energy to the dust beyond a radius of 1 pc.

We would like to thank the staff of IPAC for their help; particularly Linda Fulmer and Mehrdad Moshir, for patiently describing the *IRAS* data, and Helen Hanson and Rosanne Hernandez who cheerfully and quickly processed dozens of requests for CRDD data. This work was supported by NASA contact NAG 5-1153 and NSF contract #AST 90-15755.

References

Allen, C.W. 1973, Astrophysical Quantities (London:Athlone)

Aumann, H.H., Fowler, J.W., Melnyk, M., 1990, AJ, 99, 1674

Berruyer, N. and Frisch, H., 1983, A&A, 126, 269

Borkowski, K.J. and Sarazin, C.L., 1990, ApJ, 360, 173

Bowers, P.F. and Hagen, W. 1984, ApJ, 285, 637

Celis, L.S., 1980, A&A, 89, 145

Collison, A.J. and Fix, J.D., 1991, ApJ, 368, 545

Deguchi, S., Nakada, Y. and Sahai, R., 1990, A&A, 230, 339

Draine, B.T., 1987, unpublished supplement to Draine and Lee (1984)

Draine, B.T. and Lee, H.M., 1984, ApJ, 285, 89

Gail, H. P. and Sedlmayr, E., 1985, A&A, 148, 183

Gillet, F.C., Backman, D.E., Beichman, C. and Neugebauer, G., 1986, ApJ, 310, 842.

Goldreich, P. and Scoville, N., 1976, ApJ, 205, 144

Hawkins, G.W., 1990, A&A, 229, L5

Hawkins, G.W. and Zuckerman, B., 1991, ApJ, 374, 227

Hildebrand, H., 1983, Q. Jl. R. astr. Soc., 24, 267

Iben, I. and Renzini, A. 1983, ARA&A, 21, 271

IRAS, Point Source Catalog, 1985, US Government Publication Office

Kleinmann, S.G. 1989, Evolution of Peculiar Red Giant Stars, IAU Colloquium 106, Cambridge University Press

Knapp, G.R., Phillips, T.G., Leighton, R.B., Lo, K.Y., Wannier, P.G., and Wootten, H.A. 1982, ApJ, 252, 616

Knapp, G.R. and Morris, M. 1985, ApJ, 292, 640

Knapp, G.R. 1986, ApJ, 311, 731

Kwok, S. 1975, ApJ, 198, 583

Leene, A. and Pottasch, S.R., 1988, A&A, 202, 203

Letzelter, E., Eidelsberg, M., Rostas, F., Breton, J, and Thiebelmont, B. 1987, *Chem. Phys.* 114, 273

Low F.J. *et al.* , 1984, ApJ, 278, L19

Mamon, G.A., Glassgold, A.E. and Huggins, P.J. 1988, ApJ, 328, 797

Mihalas, D. and Binney, J., 1981, Galactic Astronomy, W. H. Freeman

Morris, M., 1980, ApJ, 236, 823

Moshir, M., *et al*, 1989, Explanatory Supplement to the IRAS Faint Source Survey, preprint

Olofsson, H., 1988, Space Science Reviews, 47, 145

Olofsson, H., Eriksson, K. and Gustafsson, B. 1987, A&A, 183, L13

Olofsson, H., Eriksson, K. and Gustafsson, B. 1988, A&A, 196, L1

Press, W.H., Flannery, B.P., Teukolsky, S.A. and Vetterling, W.A. 1986, Numerical Recipes, Cambridge University Press

Rowan-Robinson, M., Lock, T.D., Walker, D.W. and Harris, S. 1986, MNRAS, 222, 273

Soifer, B.T, 1989, *private communication*

Spitzer, L., 1978, Physical Processes in the Interstellar Medium, Wiley

Truong-Bach, Morris, D., Nguyen-Q-Rieu, and Deguchi, S., 1990, A&A, 230, 431

van der Veen, W.E.C.J., Habing, H.J., 1988, A&A, 194, 125

van der Veen, W.E.C.J. and Rugers, M., 1989, A&A, 226, 183

Wannier, P.G. and Sahai, R. 1986, ApJ, 311, 335

Wannier, P.G., Sahai, R., Andersson, B–G and Johnson, H. R., 1990, ApJ, 358, 251

Wickramasinghe, N.C., 1972, NMRAS, 159, 269

Willems, F.J., de Jong, T., 1988, 196, 173

Young, H.D., 1962, Statistical Treatment of Experimental Data, McGraw-Hill

Young, K. *et al.* 1992 *in preparation*

Zuckerman, B. and Dyck, H.M. 1986, ApJ, 304, 394

Zuckerman, B., Dyck, H.M. and Claussen, M.J. 1986, ApJ, 304, 401

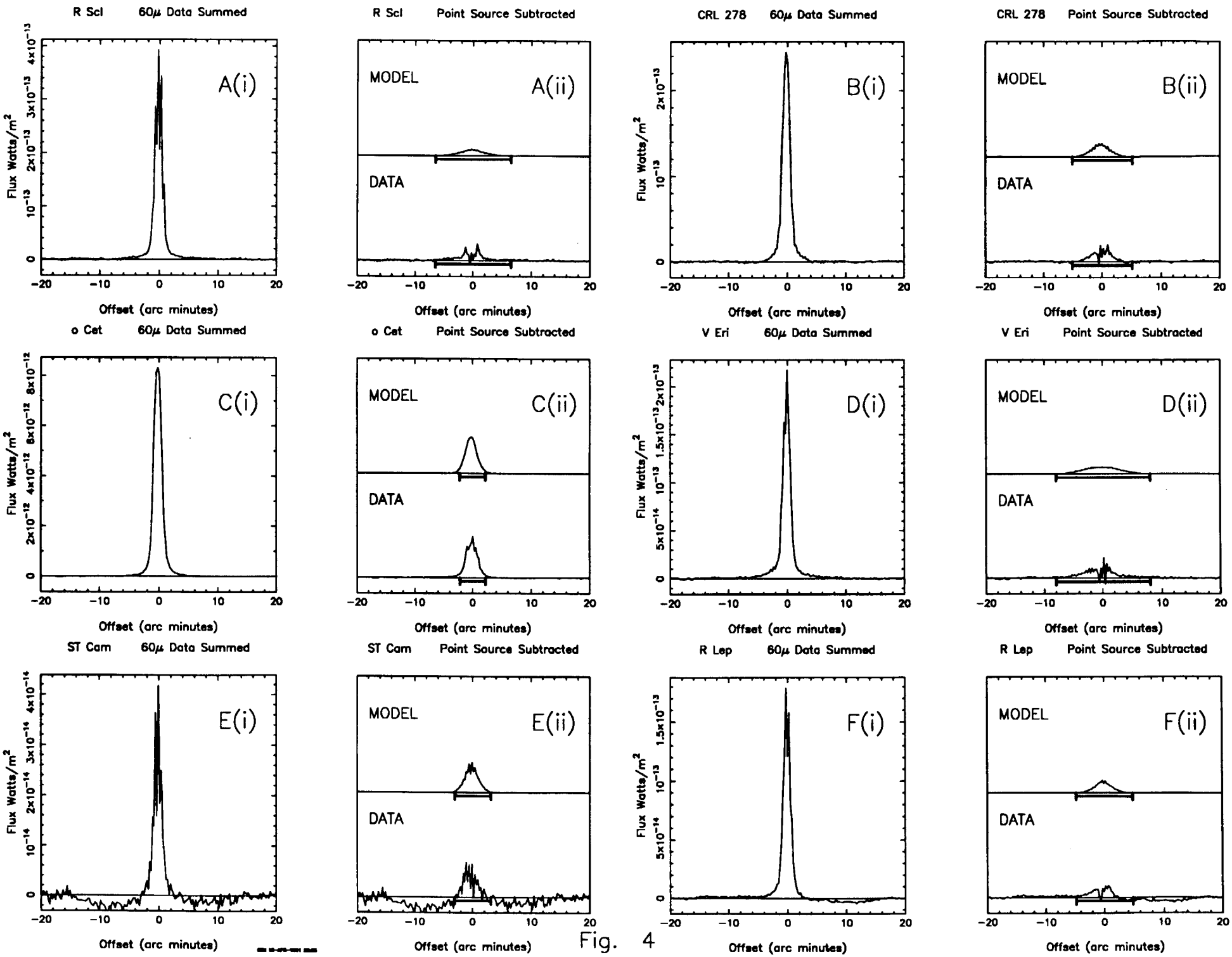
R Scl 60μ Data Summed
R Scl Point Source Subtracted
CRL 278 60μ Data Summed
CRL 278 Point Source Subtracted
A(i)
A(ii)
B(i)
B(ii)
MODEL
DATA
Flux Watts/m²
Offset (arc minutes)
o Cet 60μ Data Summed
o Cet Point Source Subtracted
V Eri 60μ Data Summed
V Eri Point Source Subtracted
C(i)
C(ii)
D(i)
D(ii)
ST Cam 60μ Data Summed
ST Cam Point Source Subtracted
R Lep 60μ Data Summed
R Lep Point Source Subtracted
E(i)
E(ii)
F(i)
F(ii)

Fig. 4

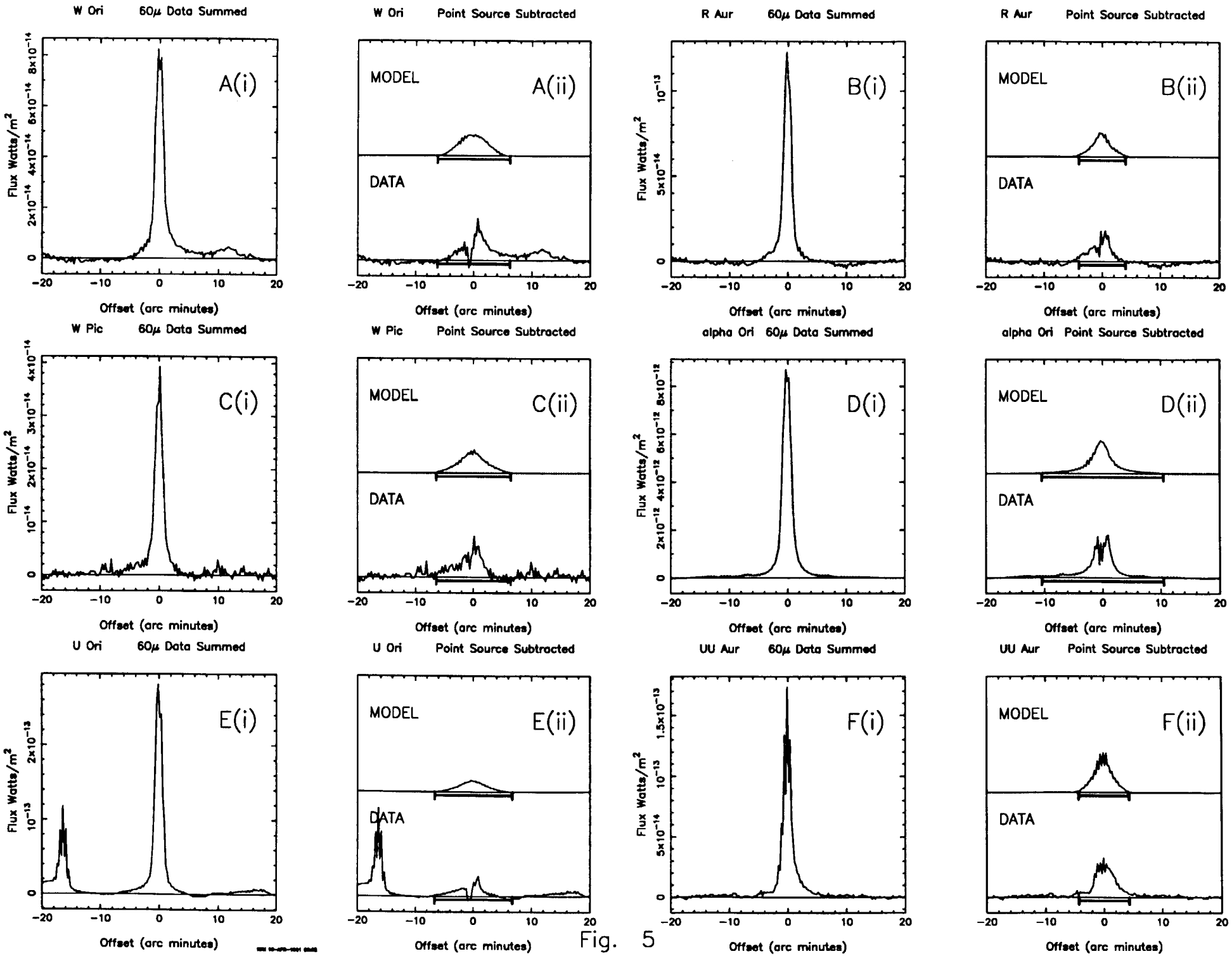
W Ori 60μ Data Summed
W Ori Point Source Subtracted
R Aur 60μ Data Summed
R Aur Point Source Subtracted
W Pic 60μ Data Summed
W Pic Point Source Subtracted
alpha Ori 60μ Data Summed
alpha Ori Point Source Subtracted
U Ori 60μ Data Summed
U Ori Point Source Subtracted
UU Aur 60μ Data Summed
UU Aur Point Source Subtracted
A(i)
A(ii)
B(i)
B(ii)
C(i)
C(ii)
D(i)
D(ii)
E(i)
E(ii)
F(i)
F(ii)
MODEL
DATA
Flux Watts/m²
Offset (arc minutes)

Fig. 5

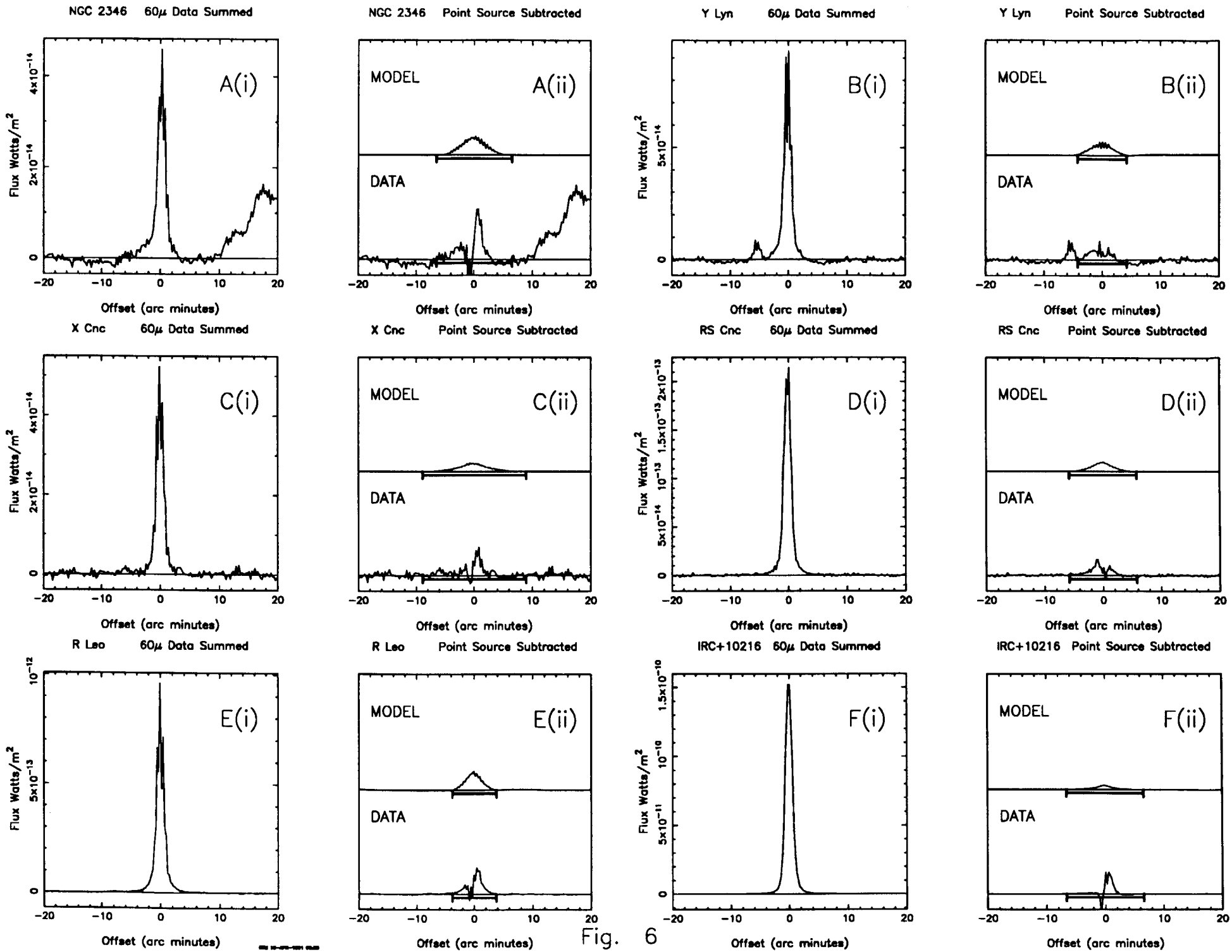
NGC 2346 60μ Data Summed
NGC 2346 Point Source Subtracted
Y Lyn 60μ Data Summed
Y Lyn Point Source Subtracted
A(i)
A(ii)
B(i)
B(ii)
MODEL
DATA
Flux Watts/m²
Offset (arc minutes)
X Cnc 60μ Data Summed
X Cnc Point Source Subtracted
RS Cnc 60μ Data Summed
RS Cnc Point Source Subtracted
C(i)
C(ii)
D(i)
D(ii)
R Leo 60μ Data Summed
R Leo Point Source Subtracted
IRC+10216 60μ Data Summed
IRC+10216 Point Source Subtracted
E(i)
E(ii)
F(i)
F(ii)

Fig. 6

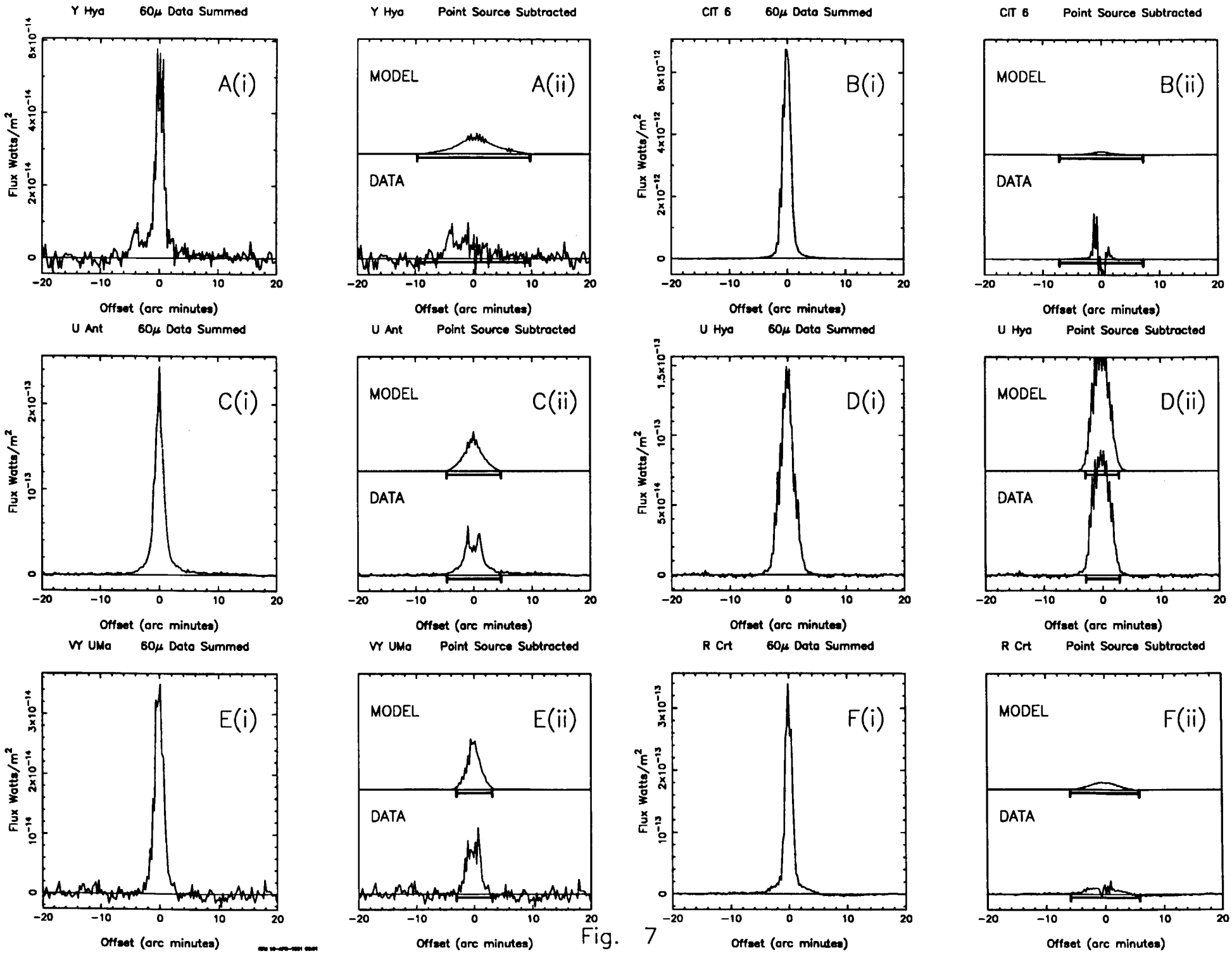
Y Hya 60μ Data Summed
A(i)
Flux Watts/m²
Offset (arc minutes)
Y Hya Point Source Subtracted
MODEL
A(ii)
DATA
Offset (arc minutes)
CIT 6 60μ Data Summed
B(i)
Flux Watts/m²
Offset (arc minutes)
CIT 6 Point Source Subtracted
MODEL
B(ii)
DATA
Offset (arc minutes)
U Ant 60μ Data Summed
C(i)
Flux Watts/m²
Offset (arc minutes)
U Ant Point Source Subtracted
MODEL
C(ii)
DATA
Offset (arc minutes)
U Hya 60μ Data Summed
D(i)
Flux Watts/m²
Offset (arc minutes)
U Hya Point Source Subtracted
MODEL
D(ii)
DATA
Offset (arc minutes)
VY UMa 60μ Data Summed
E(i)
Flux Watts/m²
Offset (arc minutes)
VY UMa Point Source Subtracted
MODEL
E(ii)
DATA
Offset (arc minutes)
R Crt 60μ Data Summed
F(i)
Flux Watts/m²
Offset (arc minutes)
R Crt Point Source Subtracted
MODEL
F(ii)
DATA
Offset (arc minutes)

Fig. 7

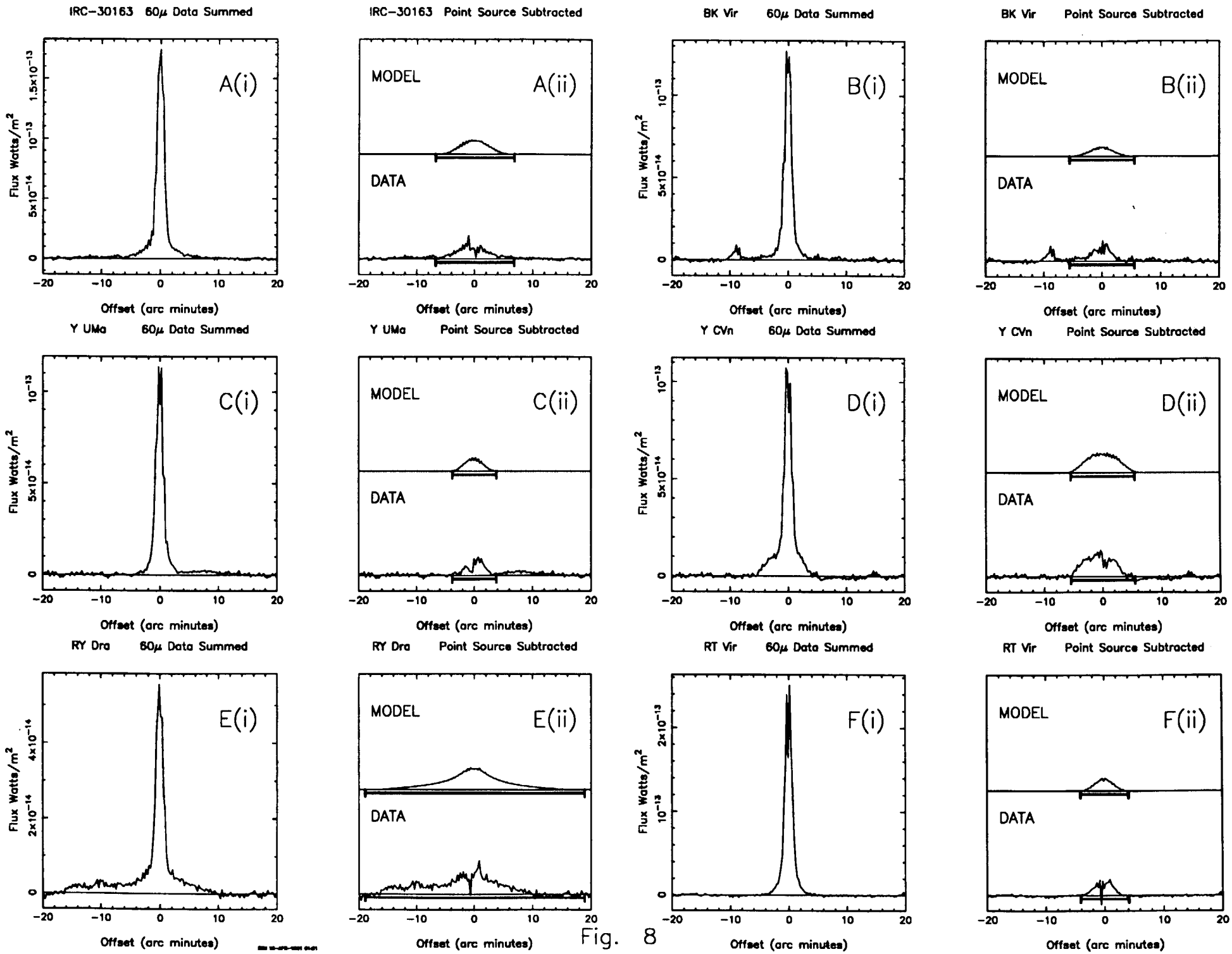
IRC-30163 60μ Data Summed
A(i)
Flux Watts/m²
Offset (arc minutes)
IRC-30163 Point Source Subtracted
MODEL
A(ii)
DATA
Offset (arc minutes)
BK Vir 60μ Data Summed
B(i)
Offset (arc minutes)
BK Vir Point Source Subtracted
MODEL
B(ii)
DATA
Offset (arc minutes)
Y UMa 60μ Data Summed
C(i)
Offset (arc minutes)
Y UMa Point Source Subtracted
MODEL
C(ii)
DATA
Offset (arc minutes)
Y CVn 60μ Data Summed
D(i)
Offset (arc minutes)
Y CVn Point Source Subtracted
MODEL
D(ii)
DATA
Offset (arc minutes)
RY Dra 60μ Data Summed
E(i)
Offset (arc minutes)
RY Dra Point Source Subtracted
MODEL
E(ii)
DATA
Offset (arc minutes)
RT Vir 60μ Data Summed
F(i)
Offset (arc minutes)
RT Vir Point Source Subtracted
MODEL
F(ii)
DATA
Offset (arc minutes)

Fig. 8

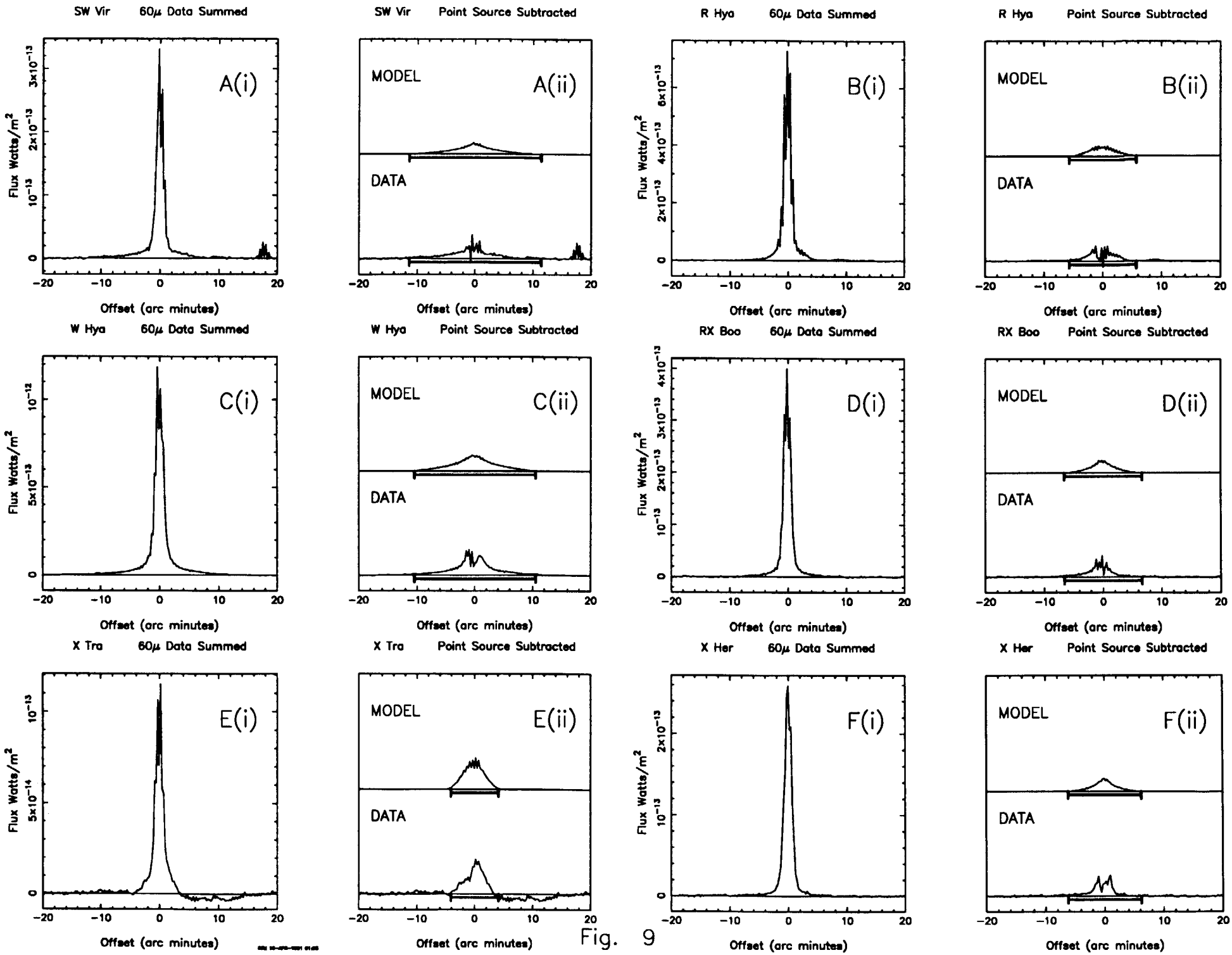
SW Vir 60μ Data Summed
A(i)
SW Vir Point Source Subtracted
MODEL
A(ii)
DATA
R Hya 60μ Data Summed
B(i)
R Hya Point Source Subtracted
MODEL
B(ii)
DATA
W Hya 60μ Data Summed
C(i)
W Hya Point Source Subtracted
MODEL
C(ii)
DATA
RX Boo 60μ Data Summed
D(i)
RX Boo Point Source Subtracted
MODEL
D(ii)
DATA
X Tra 60μ Data Summed
E(i)
X Tra Point Source Subtracted
MODEL
E(ii)
DATA
X Her 60μ Data Summed
F(i)
X Her Point Source Subtracted
MODEL
F(ii)
DATA
Flux Watts/m²
Offset (arc minutes)

Fig. 9

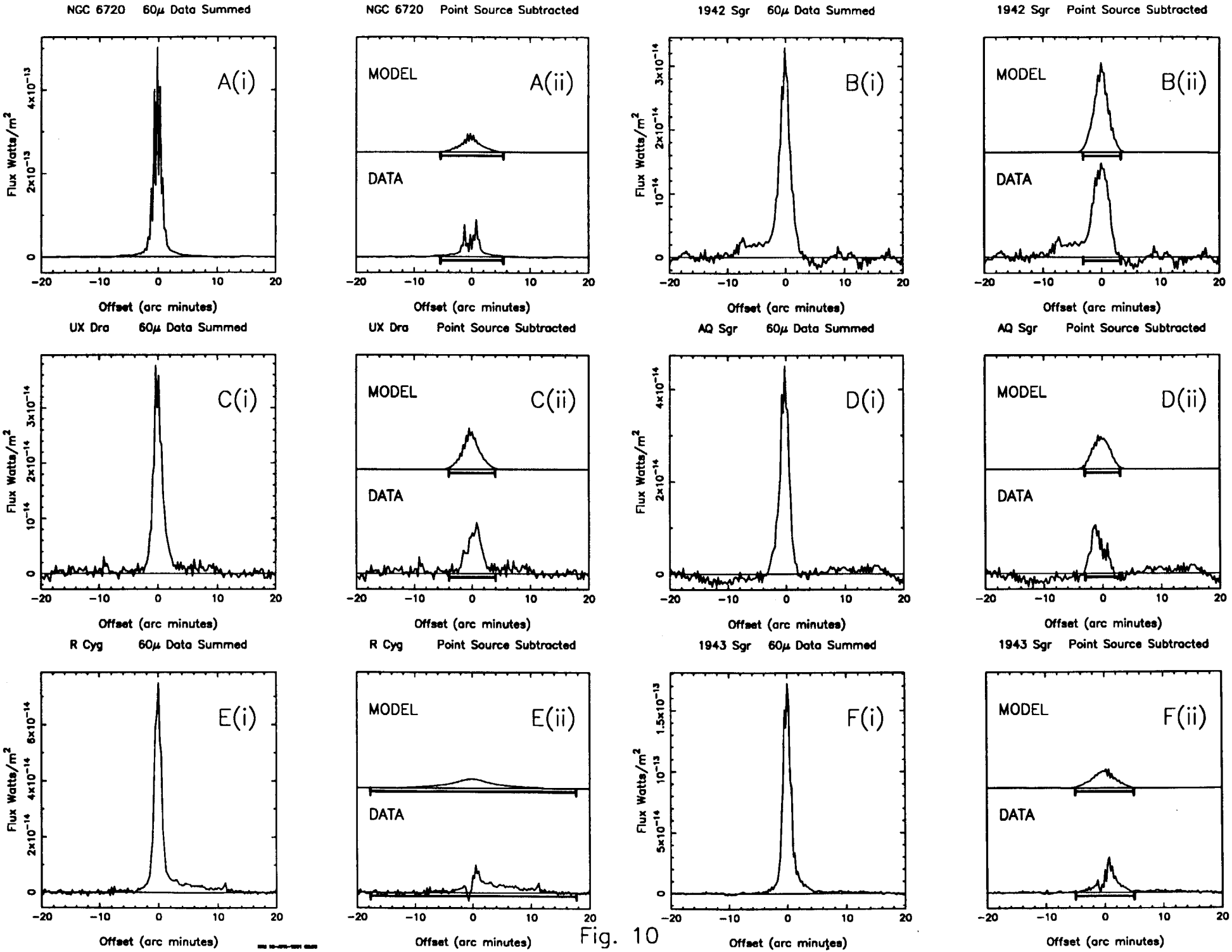
NGC 6720 60μ Data Summed
A(i)
NGC 6720 Point Source Subtracted
MODEL
A(ii)
DATA
1942 Sgr 60μ Data Summed
B(i)
1942 Sgr Point Source Subtracted
MODEL
B(ii)
DATA
UX Dra 60μ Data Summed
C(i)
UX Dra Point Source Subtracted
MODEL
C(ii)
DATA
AQ Sgr 60μ Data Summed
D(i)
AQ Sgr Point Source Subtracted
MODEL
D(ii)
DATA
R Cyg 60μ Data Summed
E(i)
R Cyg Point Source Subtracted
MODEL
E(ii)
DATA
1943 Sgr 60μ Data Summed
F(i)
1943 Sgr Point Source Subtracted
MODEL
F(ii)
DATA
Flux Watts/m²
Offset (arc minutes)

Fig. 10

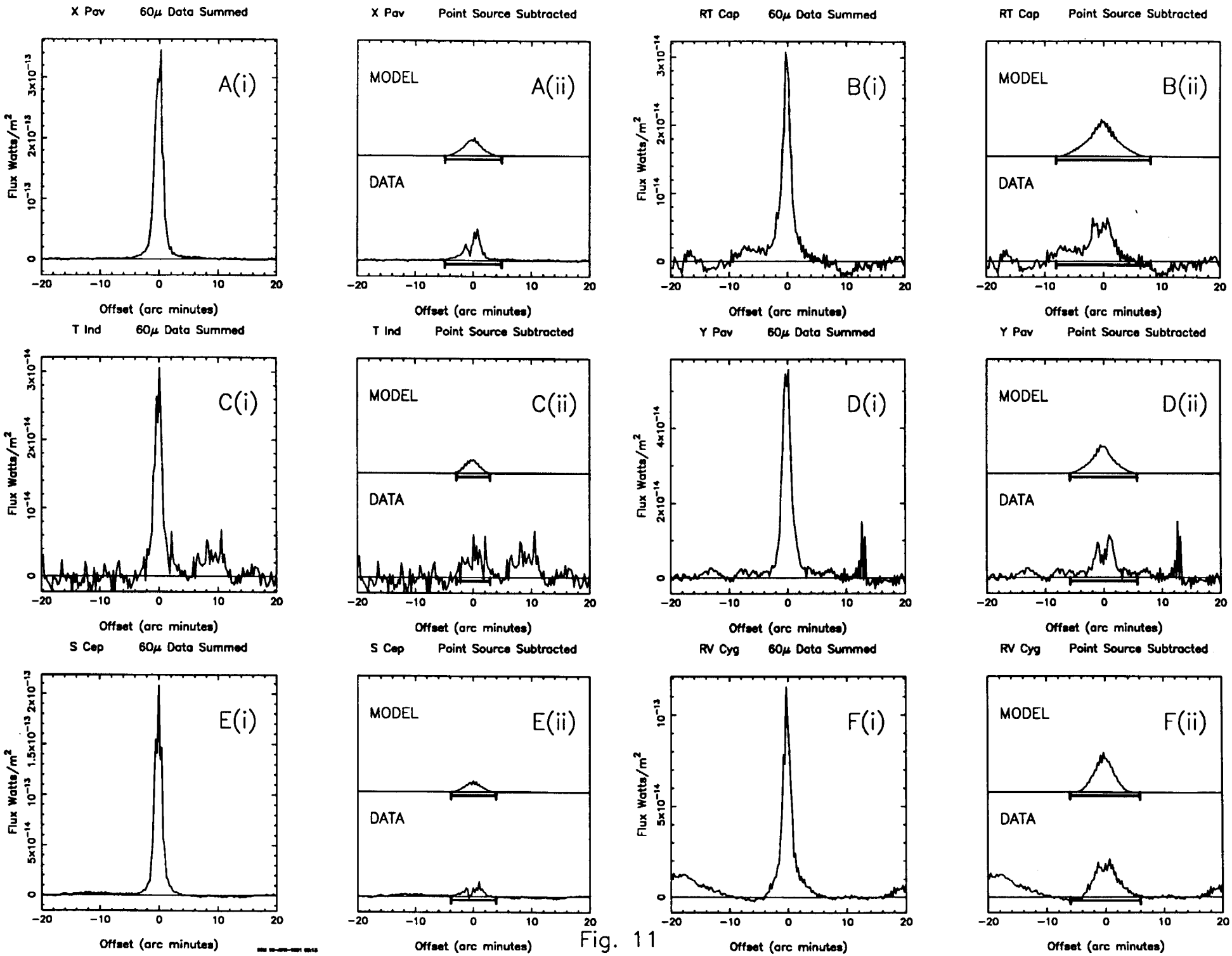
X Pav 60μ Data Summed
X Pav Point Source Subtracted
RT Cap 60μ Data Summed
RT Cap Point Source Subtracted
A(i)
A(ii)
B(i)
B(ii)
MODEL
DATA
Flux Watts/m²
Offset (arc minutes)
T Ind 60μ Data Summed
T Ind Point Source Subtracted
Y Pav 60μ Data Summed
Y Pav Point Source Subtracted
C(i)
C(ii)
D(i)
D(ii)
S Cep 60μ Data Summed
S Cep Point Source Subtracted
RV Cyg 60μ Data Summed
RV Cyg Point Source Subtracted
E(i)
E(ii)
F(i)
F(ii)

Fig. 11

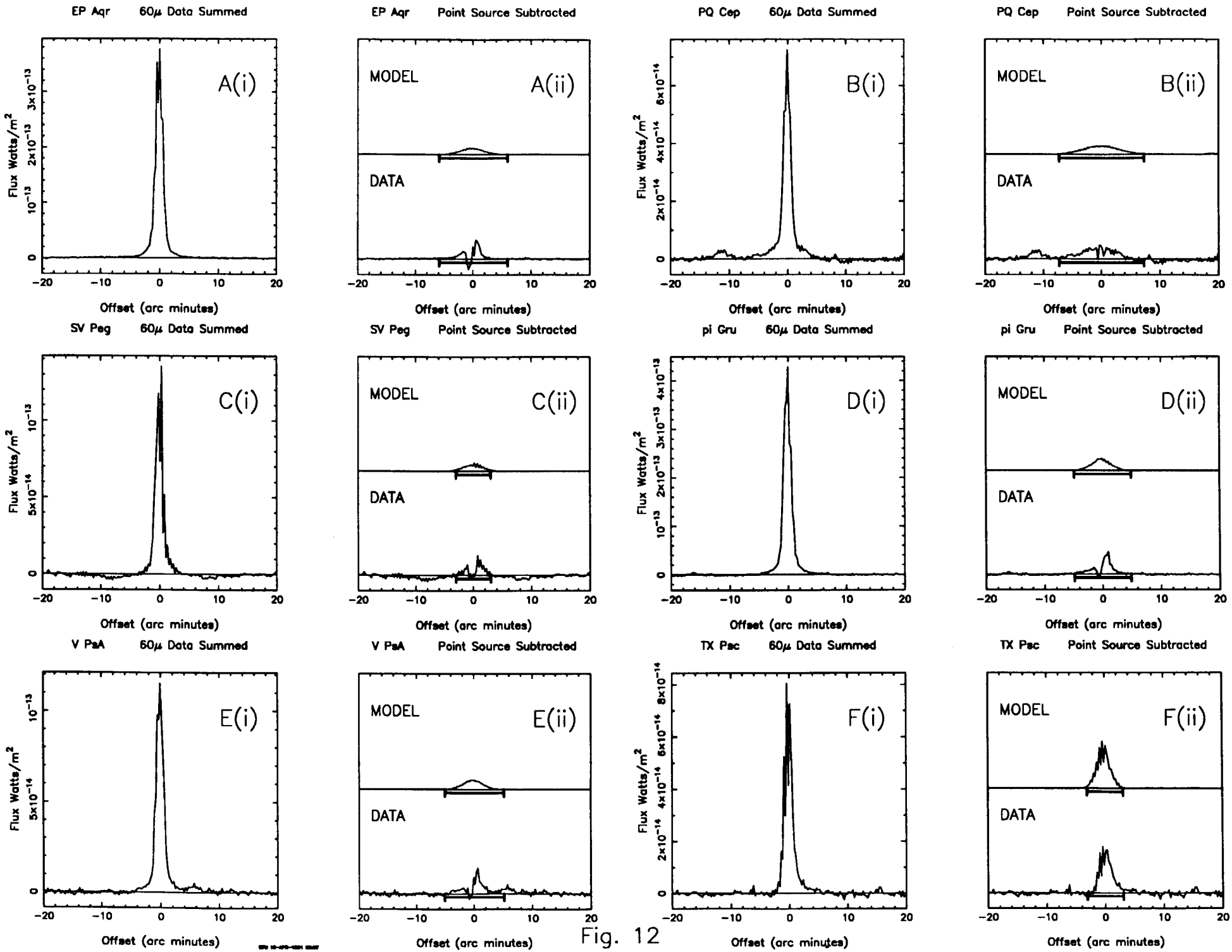
EP Aqr 60μ Data Summed
A(i)
EP Aqr Point Source Subtracted
MODEL
A(ii)
DATA
PQ Cep 60μ Data Summed
B(i)
PQ Cep Point Source Subtracted
MODEL
B(ii)
DATA
SV Peg 60μ Data Summed
C(i)
SV Peg Point Source Subtracted
MODEL
C(ii)
DATA
pi Gru 60μ Data Summed
D(i)
pi Gru Point Source Subtracted
MODEL
D(ii)
DATA
V PsA 60μ Data Summed
E(i)
V PsA Point Source Subtracted
MODEL
E(ii)
DATA
TX Psc 60μ Data Summed
F(i)
TX Psc Point Source Subtracted
MODEL
F(ii)
DATA
Flux Watts/m²
Offset (arc minutes)

Fig. 12

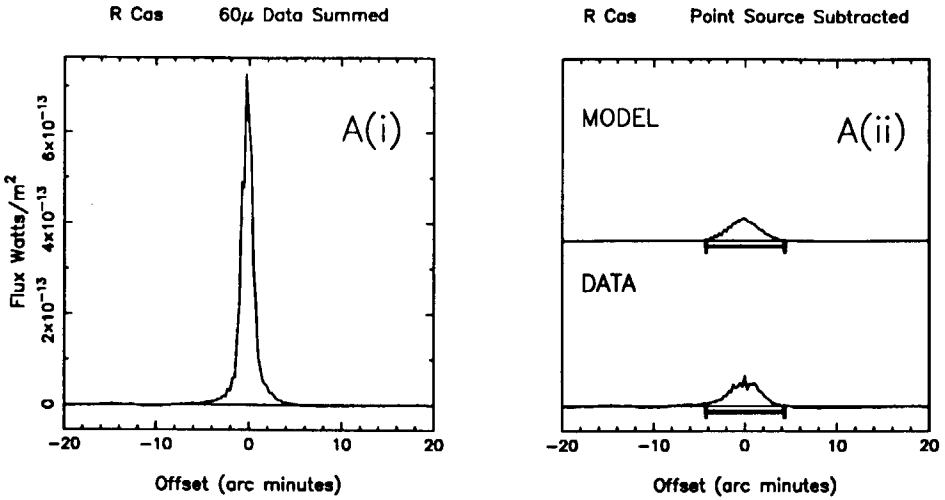
R Cas
60μ Data Summed
A(i)
Flux Watts/m²
0
2x10⁻¹³
4x10⁻¹³
6x10⁻¹³
−20
−10
0
10
20
Offset (arc minutes)
R Cas
Point Source Subtracted
MODEL
A(ii)
DATA
−20
−10
0
10
20
Offset (arc minutes)

Fig 13

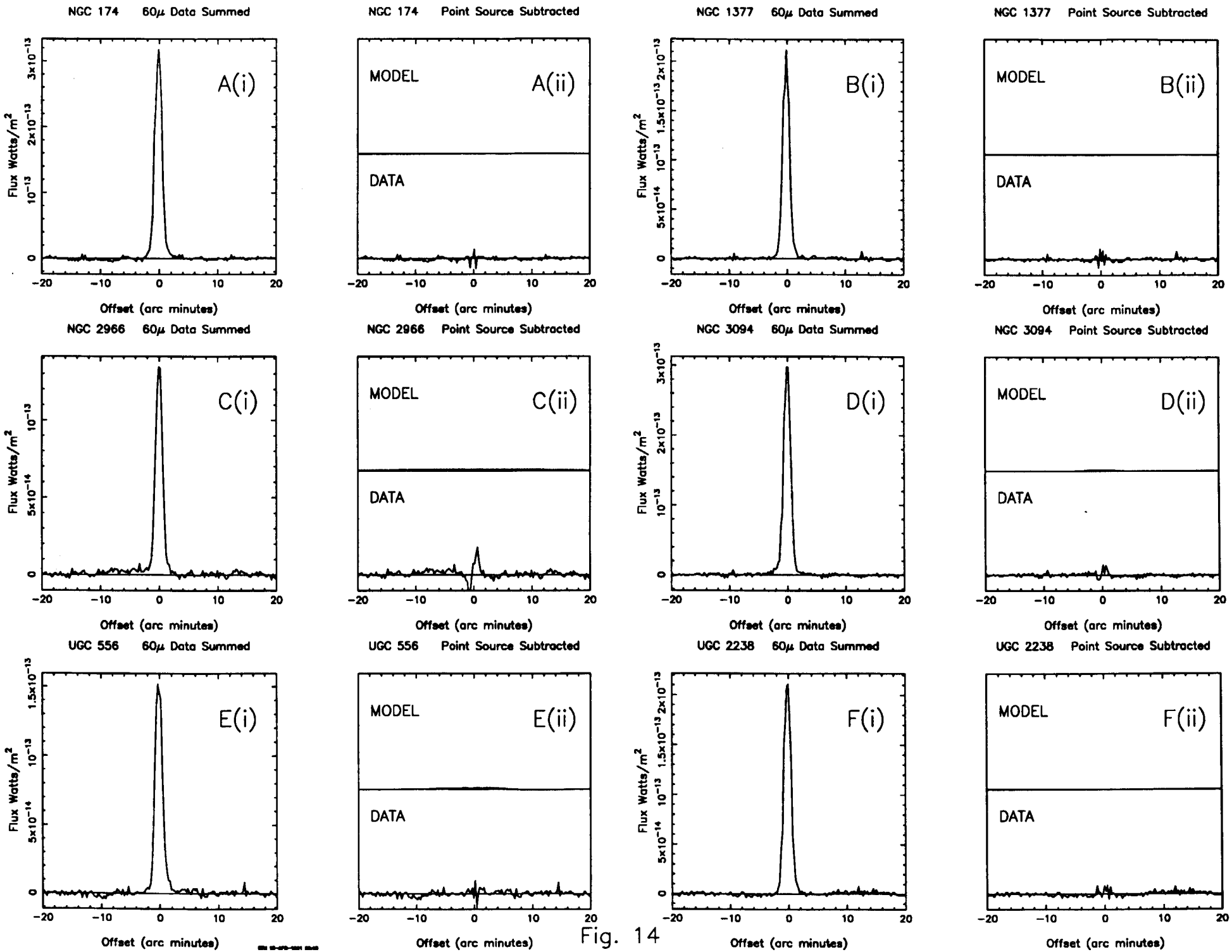
NGC 174 60μ Data Summed
NGC 174 Point Source Subtracted
NGC 1377 60μ Data Summed
NGC 1377 Point Source Subtracted
A(i)
A(ii)
B(i)
B(ii)
MODEL
DATA
Flux Watts/m²
Offset (arc minutes)
NGC 2966 60μ Data Summed
NGC 2966 Point Source Subtracted
NGC 3094 60μ Data Summed
NGC 3094 Point Source Subtracted
C(i)
C(ii)
D(i)
D(ii)
UGC 556 60μ Data Summed
UGC 556 Point Source Subtracted
UGC 2238 60μ Data Summed
UGC 2238 Point Source Subtracted
E(i)
E(ii)
F(i)
F(ii)

Fig. 14

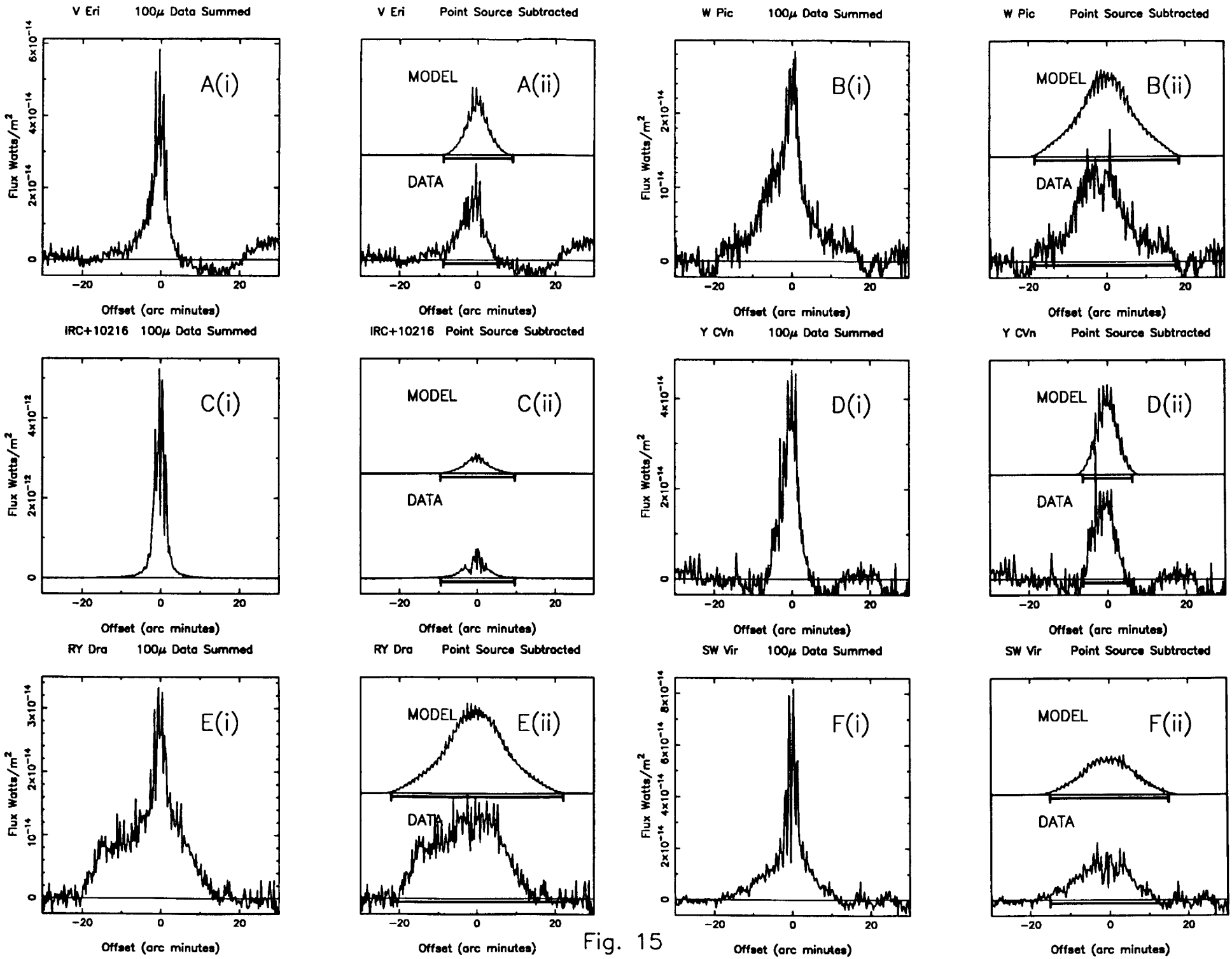
V Eri 100μ Data Summed
A(i)
V Eri Point Source Subtracted
MODEL
A(ii)
DATA
W Pic 100μ Data Summed
B(i)
W Pic Point Source Subtracted
MODEL
B(ii)
DATA
IRC+10216 100μ Data Summed
C(i)
IRC+10216 Point Source Subtracted
MODEL
C(ii)
DATA
Y CVn 100μ Data Summed
D(i)
Y CVn Point Source Subtracted
MODEL
D(ii)
DATA
RY Dra 100μ Data Summed
E(i)
RY Dra Point Source Subtracted
MODEL
E(ii)
DATA
SW Vir 100μ Data Summed
F(i)
SW Vir Point Source Subtracted
MODEL
F(ii)
DATA
Flux Watts/m²
Offset (arc minutes)
-20
0
20

Fig. 15

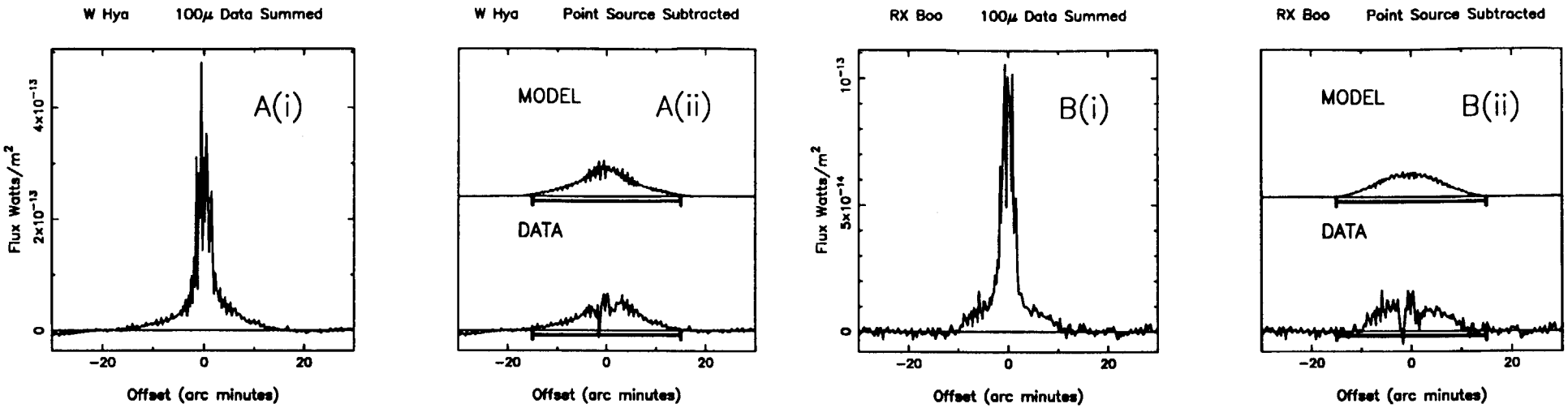
W Hya 100μ Data Summed
A(i)
Flux Watts/m²
4x10⁻¹³
2x10⁻¹³
0
-20
0
20
Offset (arc minutes)
W Hya Point Source Subtracted
MODEL
A(ii)
DATA
-20
0
20
Offset (arc minutes)
RX Boo 100μ Data Summed
B(i)
Flux Watts/m²
10⁻¹³
5x10⁻¹⁴
0
-20
0
20
Offset (arc minutes)
RX Boo Point Source Subtracted
MODEL
B(ii)
DATA
-20
0
20
Offset (arc minutes)

Fig 16